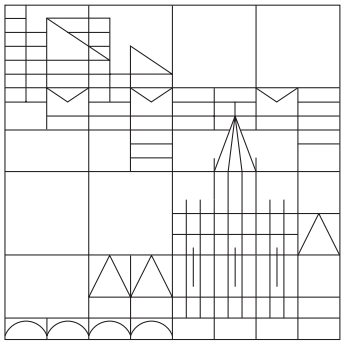

University of Konstanz

Department of Physics

Diploma Thesis

Implementation of an Apertureless Scanning Near-Field Optical Microscope for the Infrared Spectrum

Jens Dorfmüller

March 2006

Zusammenfassung

In dieser Arbeit wird ein neues, aperturloses, nahfeldoptisches Mikroskop beschrieben, das optische Eigenschaften einer Oberfläche mit einer besseren Auflösung als 50 nm in einem großen, infraroten Spektralbereich messen kann.

Um das hohe Auflösungsvermögen jenseits der Beugungsbegrenzung zu erreichen, wird das lokale elektromagnetische Feld mit der scharfen Spitze eines Rasterkraftmikroskops (RKM) untersucht. Ein Dauerstrich-Laser wird auf die metallbeschichtete oder dielektrische Spitze des RKM, die einen Apex-Radius von ungefähr 10 nm hat, fokussiert. Ein Referenzstrahl mit der selben Wellenlänge wird zu dem zurückgestreuten Licht gemischt und wird danach von einer InSb-Diode detektiert. Dieses interferometrische System verstärkt das Signal und ermöglicht die Messung der Amplitude und der Phase des zurückgestreuten Lichts. Das gemessene Signal wird zum einen von dem Nahfeld-Information tragenden, in der Nähe des Apex gestreuten Lichts, beeinflusst. Zum größeren Teil besteht das Signal aber aus einer Hintergrundkomponente, die von Licht herrührt, das am Rest der Spitze und der Probe gestreut wurde. Um das Hintergrundsignal zu unterdrücken, wird das RKM im Nicht-Kontakt-Modus mit kleiner Schwingungsamplitude verwendet und das gemessene Signal mit einem Lock-In-Verstärker bei einer höheren Harmonischen der Schwingungsfrequenz der Spitze demoduliert. Durch das Abrastern der Probe unter der Spitze werden Informationen sowohl über das Nahfeld als auch die Topografie der Probe gewonnen.

Die Abdeckung eines großen Spektralbereichs wird durch einen Dauerstrahl-optisch-parametrischen-Oszillator (OPO) als Lichtquelle erreicht. Der OPO wurde genau charakterisiert und verleiht dem Instrument die Fähigkeit, in einem Wellenlängenbereich von 1.5 bis 3.8 μm, mit einer kleinen Lücke zwischen 2.0 und 2.3 μm, Bilder aufzunehmen. Durch die Verwendung von sphärischen Spiegeln statt Linsen ist der Aufbau nahezu achromatisch.

Um die Funktionsfähigkeit des neuen Instruments nachzuweisen, werden zwei Glasproben mit Goldstrukturen, die kleiner als die Wellenlänge sind, untersucht. Mit der ersten Probe, einer Testprobe, wird gezeigt, dass das Instrument die Fähigkeit besitzt, Materialkontrast mit einer besseren Auflösung als 50 nm abzubilden. Als

Zweites werden Split-Ring-Resonatoren, die bei der Forschung nach Materialien mit negativem Brechungsindex von Interesse sind, untersucht. Das Mikroskop zeigt dabei seine Fähigkeit, die optischen Nahfelder von plasmonisch resonanten Strukturen zu kartographieren.

Abstract

In this thesis, a new apertureless scanning near-field optical microscope (aSNOM) with the ability to resolve optical properties of surfaces with a lateral resolution better than 50 nm in a broadband infrared (IR) spectrum is described.

The high resolution beyond the diffraction limit is achieved by using the sharp tip of an atomic force microscope (AFM) to probe the local electromagnetic field of a sample situated at nanometer distance. A continuous wave (cw) laser beam is focused onto the apex of a metalized or dielectric AFM tip with an apex radius of about 10 nm. The backscattered light is mixed with a reference beam of the same wavelength and detected with a nitrogen cooled InSb-photovoltaic diode. This interferometric scheme allows to enhance the signal level and to detect both the amplitude and phase of the scattered light. The obtained signal is influenced by two components: the light scattered in a small vicinity of the tip apex containing near-field information from the sample, and a background field scattered from the body of the tip and from the sample. To suppress the background component, the AFM is used in non-contact mode with a small vibration amplitude, and the signal is demodulated at higher harmonics of the tip vibration frequency with a lock-in amplifier. By raster scanning the sample under the AFM tip, near-field information from the sample is obtained simultaneously with the topography.

Imaging in a broad infrared spectrum is achieved by using a cw optical parametric oscillator (cw-OPO) as light source. The OPO has been carefully characterized and gives the instrument the capability to image in a spectral region from 1.5 to 3.8 μm with a small gap between 2.0 and 2.3 μm. By using spherical mirrors instead of lenses, the setup is nearly achromatic.

As applications of the infrared aSNOM (IR-aSNOM), images of two different sub-wavelength gold structures on glass surfaces were taken. The first is a test sample that shows the capability of the instrument to image material contrast with a lateral resolution better than 50 nm, corresponding to $\lambda/50$. The second application shown is the investigation of split-ring resonators, which are of interest for the study of negative index materials. Maps of optical near-fields at the resonantly excited plasmonic structures are shown — with similar resolution.

Contents

1 Introduction

The optical microscope is one of the best-known scientific instruments. Almost anyone has an idea what a "microscope" is, at least the usual optical microscope. It deserves its reputation because the optical microscope has advanced science for many centuries. However, while it continues to be a valuable tool in science, the usual optical microscope is not suitable anymore for scientists reaching out to the nano-world.

At the end of the 18th century already, Abbé and Lord Rayleigh showed that the spatial resolution of such microscopes is limited. The well-known *Abbé diffraction limit* states that objects less than about half a wavelength apart cannot be represented separately. The achievable resolution of about 200 nm is still good enough to map many features inside a cell (size $\approx$ 10 µm) but not good enough to get an insight into the interior workings of these features. Other types of microscopes, such as the scanning electron microscope (SEM) or the scanning tunneling microscope (STM), can achieve a much higher resolution but are not suitable for research on living non-conductive matter.

For this purpose, other types of optical microscopes have been developed. The confocal laser scanning microscope (CLSM) was developed in the 1960s. The state of the art confocal microscope is the 4π-microscope which gives a resolution of $\approx$ 100 nm ($\lambda/10$) [12]. Its disadvantage is that the sample has to be transparent.

Of course, not only biologists are interested in optical microscopy with high resolution. There are many optical phenomena at the sub-wavelength scale that are still undiscovered. To access these, techniques that are well-known from radio wave technology might lead to the equivalents of optical antennas or metallic optical waveguides when they are scaled down to submicron scale [32].

Another idea to improve the resolution of optical microscopes came from Synge [36] in the 1930s. Not until the 1980s, after the development of the STM, could his ideas be realized [27]. He proposed to squeeze light through a sub-wavelength

aperture. Placing this aperture in a distance of less than the diameter of the sample should then give a resolution comparable to the size of the aperture. But a too small aperture does not let pass enough light and the resolution of these scanning near-field optical microscopes (SNOM) is limited to about 50 nm ($\approx \lambda/20$) [14, 11].

The spatial resolution of all the previously mentioned optical microscopy techniques scales with the wavelength of the light used. This is a problem especially for infrared microscopy with its longer wavelengths. The apertureless SNOM (aSNOM), a new technique developed in the late 1990s, yields a resolution that is not proportional to the wavelength. It uses a small antenna, normally a standard atomic force microscope (AFM) tip, to probe the local electromagnetic field. As I show in chapter 2 the field enhancement between the tip and the sample offers the possibility to detect just the light from the tip apex region. With a tip apex radius of less than 10 nm this approach can give a sub-10 nm resolution even in the infrared [40, 37].

In chapter 3, I explain the setup and the components I chose. The principle I followed during the design of the infrared aSNOM (IR-aSNOM) was to keep the maximum flexibility. Finally, this lead to a setup that can be used in the infrared as well as in the visible spectrum by just exchanging the beam splitters and the detector. All the other components work on a broad spectral range from 400 nm to 10 µm. The laser used for the IR-aSNOM is somewhat of a novelty to apertureless scanning near-field optical microscopy, allowing access to over an octave of wavelengths in the near-infrared. It is tunable from 1.5 to 3.8 µm with a small gap between 2.0 and 2.3 µm. In these regions, it is not limited to single laser lines but is continuously tunable. Not only because of its tunability, the laser is an interesting light source. Many molecules show vibrational absorption in the accessible wavelength range. For example, the stretching vibrations of C-H, O-H and N-H groups are in the range between 2.5 and 4 µm. The accessible photon energy (0.32 eV to 0.83 eV) also offers access to other light-matter interactions: the band gap of many semiconductors (for example InAs: $\approx$ 0.4 eV, Ge: $\approx$ 0.7 eV) is in this range. These phenomena can show up as resonances, absorbance or just as material contrast.

Chapter 4 describes how the new instrument was tested. The first scans with a resolution of about 50 nm at a wavelength of 2.5 µm are shown in chapter 5. In chapter 6, I give an outlook for possible improvements and research activities with the IR-aSNOM planned in the future.

2 Theoretical Background

In this chapter, I give a short introduction into the theory that is commonly used to explain the principles of apertureless scanning near-field optical microscopy. The first section gives an explanation of the diffraction limit of normal microscopes and how it can be overcome. Subsequently, I present a model that explains the field enhancement between a sharp tip and a substrate in close distance. Finally, the technique of interferometric amplification of weak signals will be discussed.

2.1 Diffraction Limit

The first optical microscopes where invented in the 17th century. These instruments are still a standard tool in many parts of science, especially in biology and medical science. By the end of the 18th century, a limitation in lateral resolution of this technology was found, now known as Abbé diffraction limit. Ultimately, this limit is traced to the fact that a conventional optical microscope uses only far-field measurements to image a sample. The crucial parameter to distinguish between near-field and far-field measurements is the distance between the detector and the sample D. Measurements with a detector in the near-field ($D < \lambda$) can indeed result in much higher spatial information, as I will show below.

Figure 2.1 shows a simplified two-dimensional model of four scatterers at distances which are comparable to the wavelength. (a) shows a detector being moved parallel to the sample in a distance D also in the dimension of the wavelength. In contrast to this, figure (b) shows the detector being moved in the far-field.

This kind of situation can be described by a partial wave analysis, which expresses an arbitrary field as a linear combination of plane waves [10]. With $\boldsymbol{A}(\boldsymbol{k})$ being the amplitude of the partial wave of wavevector $\boldsymbol{k}$, the electric field $\boldsymbol{E}(\boldsymbol{r})$ at the position

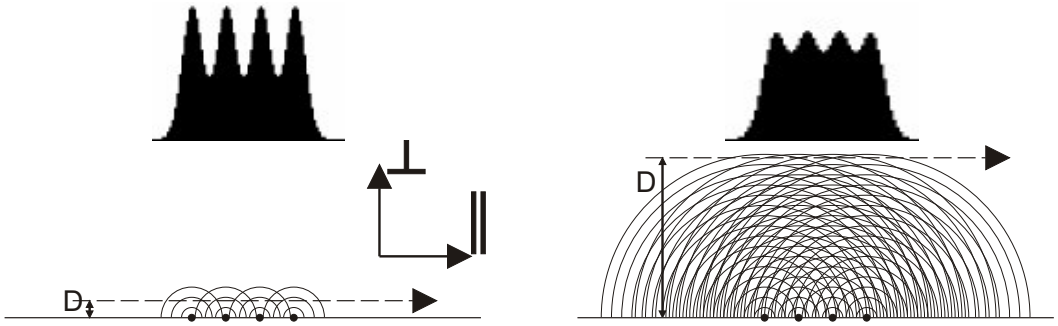

Figure 2.1: diffraction limit: a detector is moved along the dashed line. (a) shows the detector in a distance D being comparable to the wavelength, (b) shows D being larger than the wavelength

r can be written as:

$$\boldsymbol{E}(\boldsymbol{r},t) = \frac{1}{\sqrt{2\pi}^3} \iiint \mathrm{d}^3\boldsymbol{k}\, \mathrm{e}^{\imath(\boldsymbol{k}\,\cdot\,\boldsymbol{r}-\omega t)} \boldsymbol{A}(\boldsymbol{k}) \tag{2.1}$$

The dispersion relation ($\boldsymbol{k}_{(\mathrm{med})}^2 = \omega^2/c^2 = {\boldsymbol{k}_\parallel}^2 + {k_\perp}^2$) can be used to carry out the integration over $\boldsymbol{k}$. $\boldsymbol{k}_{(\mathrm{med})}$ is the wavevector magnitude of the monochromatic light used for illumination in the medium above the surface (typically air, water or oil). The remaining area integration in the $\boldsymbol{k}_\parallel$ plane is transformed into polar coordinates and the fact that the perpendicular component of the position is the distance from the detector to the sample shown in figure 2.1 is used: $r_\perp = D$.

$$\boldsymbol{E}(\boldsymbol{r},t) = \frac{1}{\sqrt{2\pi}^3} \int_0^\infty \mathrm{d}k_\parallel \int_0^{2\pi} \mathrm{d}\varphi\, k_\parallel \mathrm{e}^{\imath(k_\parallel \binom{\cos\varphi}{\sin\varphi} \cdot \boldsymbol{r}_\parallel - \omega t)} \mathrm{e}^{\imath D\sqrt{\boldsymbol{k}_{(\mathrm{med})}^2 - {k_\parallel}^2}} \boldsymbol{A}\left(k_\parallel, \varphi\right) \tag{2.2}$$

where now $k_\parallel$ is the absolute value of $\boldsymbol{k}_\parallel$ and φ is its angle. For all $k_\parallel$ bigger than $\left|\boldsymbol{k}_{(\mathrm{med})}\right|$, the root in equation 2.2 gets imaginary. Together with the $\imath$ in front of the root, it makes the whole integrand exponentially decaying for large $k_\parallel$. The exponent gets much smaller than -1 when $D\sqrt{k_\parallel^2 - \boldsymbol{k}_{(\mathrm{med})}^2} \gg 1$. This means that the electric field is well approximated by an integration over $k_\parallel$ from 0 to $k_{\max}$:

$$k_{\max} = \sqrt{D^{-2} + \boldsymbol{k}_{(\mathrm{med})}^2}. \tag{2.3}$$

For D smaller than the absolute value of the inverse wavevector, the integration is carried out over components of the wavevector with spatial frequencies up to $k_{\max} \approx D^{-1}$.

$$D \ll \left|\boldsymbol{k}_{(\mathrm{med})}\right|^{-1} \quad \Longrightarrow \quad \int_0^{\infty} \mathrm{d}k_{\parallel} \approx \int_0^{D^{-1}} \mathrm{d}k_{\parallel} \tag{2.4}$$

For large distances between the sample and the detector, the upper integration boundary can also be approximated—this time simply by the wavevector itself:

$$D \gg \left|\boldsymbol{k}_{(\mathrm{med})}\right|^{-1} \quad \Rightarrow \quad \int_0^{\infty} \mathrm{d}k_{\parallel} \approx \int_0^{|\boldsymbol{k}|} \mathrm{d}k_{\parallel} \tag{2.5}$$

This means that the spatial information carried by the high frequency waves gets lost in the far-field. This loss of information is also shown in figure 2.1. In (a) the contrast is much better than in (b).

This analysis shows that detecting in a distance above a sample which is much smaller than the wavelength can give a much higher spacial resolution. This is the basic principle of the aSNOM and related near-field optical microscopes. The AFM tip or a similar probe is brought into closest possible proximity of the sample surface, which then allows to pick up optical information with much enhanced spatial resolution.

2.2 Dipole Model

The near-field optical contrast in apertureless scanning near-field microscopy can be described by an analytical model, the so-called dipole model [23]. In this model, the tip apex is described as a small sphere with the radius R equal to the effective apex radius as shown in figure 2.2. Using a highly monochromatic laser light justifies using the so-called time-harmonic approximation, in which all time-variable field quantities are assumed to oscillate like $\mathrm{e}^{-\imath\omega t}$, where ω is the angular frequency of the laser light. With this simplification, the dielectric constant $\epsilon(\omega)$ and the conductivity $\sigma(\omega)$ can be merged into a single, complex-valued effective dielectric constant $\epsilon(\omega) = \epsilon(\omega) + \frac{\imath}{\omega}\sigma(\omega)$.

Because the tip apex and the tip-sample-distance are much smaller then the wavelength, the quasi-static approximation can be used [26]. In this approximation the field is static, so no retardation effects are taken into account. The material prop-

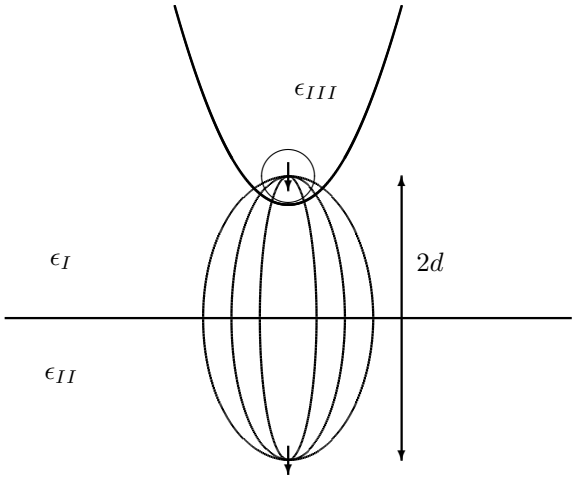

Figure 2.2: In the dipole model, the tip (dielectric constant ϵ_{III}) is approximated with a sphere of the same radius. The incident electromagnetic wave excites a dipole in the sphere. The response of the substrate underneath (dielectric constant ϵ_{II}) can be calculated with the concept of image charges. The air between the tip and the sample has the dielectric constant ϵ_I.

erties at the laser frequency are kept, but the problem is simplified to finding the electrostatic solution. The potential of a dielectric sphere over a dielectric surface can thus be solved with the aid of the well-known image charge potentials.

This analytical model describes the scattered electrical field E_s by a complex polarizability $\alpha^{(\text{eff})}$: $\boldsymbol{E}_s \propto \alpha^{(\text{eff})}\boldsymbol{E}_i$ with $\boldsymbol{E}_i$ being the incident electrical field. The total polarzability is the sum of two individual polarizabilities, ${\alpha_\parallel}^{(\text{eff})}$ for light polarized parallel to the surface, and ${\alpha_\perp}^{(\text{eff})}$ for light polarized perpendicular to the surface [2].

$$\left\{ \begin{array}{c} {\alpha_\perp}^{(\text{eff})} \\ {\alpha_\parallel}^{(\text{eff})} \end{array} \right\} = \frac{\alpha(1 \pm \beta')^2}{1 - \frac{3\pm1}{2}\frac{\alpha\beta'}{32\pi\epsilon_I d^3}} \tag{2.6}$$

with d being the distance between the center of the sphere and the substrate, $\beta' = (\epsilon_{II} - \epsilon_I)/(\epsilon_{II} + \epsilon_I)$ being the response function of the surface, and $\alpha = 4\pi R^3 \epsilon_0 (\epsilon_{III} - \epsilon_I)/(\epsilon_{III} + 2\epsilon_I)$ being the polarizability of the sphere.

Figure 2.3 shows the dependence of the polarizability ${\alpha_\perp}^{(\text{eff})}$ on the distance between the tip and the sample. The polarizability stays constant for large tip-sample distances, but increases dramatically when the distance gets smaller than the effective radius of the tip.

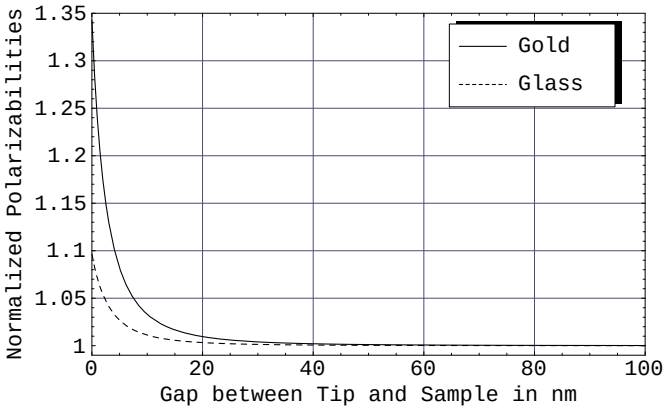

Figure 2.3: Typical static approach curve calculated using equation 2.6. The polarizability is normalized by the polarizability at a large tip sample distance individually for each graph. The tip is taken to be made of Pt, the tip radius taken as 10 nm. The dielectric constants for gold ($\epsilon = -168.2 + 23.3i$ at $\lambda = 2.066$ µm) and platinum ($\epsilon = -19.2 + 69.3i$ at $\lambda = 2.066$ µm) were taken from [25]: the one for glass ($\epsilon = 2.07$ at $\lambda = 2.058$ µm) was taken from [31].

The comparison between the graph for a gold and for a glass surface also shows that a much larger scattering signal can be expected from the gold-platinum than from the glass-platinum system. This material contrast originates from the response function of the surface $\beta'(\epsilon_{II})$.

The dipole model explains the field enhancement that makes apertureless scanning near-field optical microscopy feasible by a strong interaction between the tip and the sample. The field enhancement at the surface shown in figure 2.3 only occurs when the tip is present. Consequently we call this the "active" mode of the aSNOM. An already locally enhanced electromagnetic field near the surface offers the possibility of using the aSNOM in "passive" mode. A strong field near the surface can emerge at nano-structured surfaces. Here, the tip apex can be used to simply couple out a fraction of the existing electromagnetic field. In this case, a strong interaction between the tip and the sample is undesirable, and the tip material should be chosen to give a small polarizability α, for example, ultrasharp SiO_x-coated Si tips or even carbon nanotube attached to an AFM cantilever.

2.3 Interferometric Signal Amplification

The rather weak signal coming back from the tip-sample system is in the pico watt range. Therefore, interferometric signal amplification is convenient to boost the detectable signal. Consider two monochromatic electromagnetic fields overlapping at the detector, the field of the reference path $E^{(\mathrm{ref})}$ and the field of the signal path $E^{(\mathrm{sig})}$:

$$\boldsymbol{E}^{(\mathrm{sig})} = \boldsymbol{E}_0{}^{(\mathrm{sig})} \mathrm{e}^{\imath(\omega^{(\mathrm{sig})}t+\varphi^{(\mathrm{sig})})} \tag{2.7}$$

$$\boldsymbol{E}^{(\mathrm{ref})} = \boldsymbol{E}_0{}^{(\mathrm{ref})} \mathrm{e}^{\imath(\omega^{(\mathrm{ref})}t+\varphi^{(\mathrm{ref})})} \tag{2.8}$$

$\boldsymbol{E}_0{}^{(\mathrm{sig})}$ and $\boldsymbol{E}_0{}^{(\mathrm{ref})}$ are the amplitudes, $\omega^{(\mathrm{sig})}$ and $\omega^{(\mathrm{ref})}$ the frequencies, and $\varphi^{(\mathrm{sig})}$ and $\varphi^{(\mathrm{ref})}$ the phases of the fields.

Two ways of interferometric amplification are possible: homodyne and heterodyne. In the heterodyne version, one of the electromagnetic fields is frequency-shifted with respect to the other. Due to the lack of appropriate commercial devices to achieve this in the infrared, a homodyne version of the IR-aSNOM is used where the frequencies of the electromagnetic fields are equal: $\omega^{(\mathrm{sig})} = \omega^{(\mathrm{ref})} = \omega$.

The interferometric sum field $\boldsymbol{E}$ of these two fields results in a detected intensity I:

$$I = |\boldsymbol{E}|^2 = I^{(\mathrm{sig})} + I^{(\mathrm{ref})} + 2\,\mathrm{Re}\left(\boldsymbol{E}_0{}^{(\mathrm{sig})} \cdot \overline{\boldsymbol{E}_0{}^{(\mathrm{ref})}} \mathrm{e}^{\imath\Delta\varphi}\right) \tag{2.9}$$

where $I^{(\mathrm{sig})} = \boldsymbol{E}_0{}^{(\mathrm{sig})} \cdot \overline{\boldsymbol{E}_0{}^{(\mathrm{sig})}}$ is the intensity of the signal beam, $I^{(\mathrm{ref})} = \boldsymbol{E}_0{}^{(\mathrm{ref})} \cdot \overline{\boldsymbol{E}_0{}^{(\mathrm{ref})}}$ is the intensity of the reference beam and $\Delta\varphi = \varphi^{(\mathrm{sig})} - \varphi^{(\mathrm{ref})}$ is the phase difference between the signal and the reference beam.

In the IR-aSNOM $\boldsymbol{E}^{(\mathrm{sig})}$ is the E-field component of the backscattered light. Because the AFM-tip is vibrating in the focused beam, the backscattered light is modulated with the vibration frequency of the tip Ω. To be measured is the amplitude of the modulation of $\boldsymbol{E}^{(\mathrm{sig})}$. Therefore, the detected signal is routed into a lock-in amplifier which measures only the AC part of the signal and suppresses the DC components $I^{(\mathrm{sig})}$ and $I^{(\mathrm{ref})}$.

The signal strength $S(\Delta\varphi)$ measured with the lock-in amplifier strongly depends on the phase difference between the signal and the reference beam $\Delta\varphi$. This can

vary with time, for example by thermal effects on the path length difference such as an expansion of the base plate (see section 3.4.3). To be able to measure the full signal, the lock-in signal is measured twice at a phase difference between the signal and the reference beam of $\Delta\varphi$ and at $\Delta\varphi + \pi/2$. This is done by making the reference path by $\lambda/4$ longer using a retro-reflector (see section 3.4.5).

With the two measured values $S(\Delta\varphi)$ and $S(\Delta\varphi+\pi/2)$, it is possible to calculate the actual signal strength S:

$$S = \sqrt{S(\Delta\varphi)^2 + S(\Delta\varphi + \pi/2)^2} \tag{2.10}$$

$$\propto 2\sqrt{I^{(\mathrm{sig})}}\sqrt{I^{(\mathrm{ref})}} \tag{2.11}$$

The phase difference $\Delta\varphi$ is calculated as the total angle in the imaginary plane of $\boldsymbol{E}_0{}^{(\mathrm{sig})} \cdot \overline{\boldsymbol{E}_0{}^{(\mathrm{ref})}} \mathrm{e}^{\imath\Delta\varphi}$:

$$\psi = \arctan \frac{S(\Delta\varphi + \pi/2)}{S(\Delta\varphi)} \tag{2.12}$$

Equation 2.11 shows how the reference beam can be used to amplify the weak signal. Mixing a signal of, for example, 1 nW with a reference beam of 1 mW results in a measured signal of 2 µW. The interferometric amplification is limited by the range of the linearity of the detector. When the detector is used in the non-linear range[1], the interferometric amplification is non-linear as well.

Another effect of the interferometric amplification is the reduction of the dynamic range: signals ranging over four orders of magnitude (for example from 10^{-11} to 10^{-7} W) are mapped into a range of only two orders of magnitude (10^{-7} to 10^{-5} W when mixed with $I^{(\mathrm{ref})} = 0.25 \cdot 10^{-3}$ W).

In an aSNOM, the signal $I^{(\mathrm{sig})}$ is the power of the light scattered back from the tip, most importantly from the apex of the tip. The intensity of the backscattered light depends on the electric field strength at the apex of the tip $\boldsymbol{E} \propto \sqrt{I^{(\mathrm{sig})}}$. For small variation of the tip-sample distance, $\boldsymbol{E}$ can be expanded into a Taylor series around the mean position of the tip d_r. The position of the AFM-tip is modulated sinusoidally around its mean position with amplitude D and tip vibration frequency Ω: $d(t) = d_r + D\sin\Omega t$. In total, this results in the following expression for the

[1] when $I^{(\mathrm{ref})}$ is too large and begins to saturate the detector

electric field:

$$\boldsymbol{E}(t) = \boldsymbol{E}^{(0)} + \boldsymbol{E}^{(1)} D \sin \Omega t + \frac{1}{2}\boldsymbol{E}^{(2)} D^2 \sin^2 \Omega t + \frac{1}{6}\boldsymbol{E}^{(3)} D^3 \sin^3 \Omega t \cdots \quad (2.13)$$

$$\approx \boldsymbol{E}^{(0)} + \boldsymbol{E}^{(1)} D \sin \Omega t - \frac{1}{2}\boldsymbol{E}^{(2)} D^2 \cos 2\Omega t - \frac{1}{24}\boldsymbol{E}^{(3)} D^3 \sin 3\Omega t + \cdots \quad (2.14)$$

where $\left\{\boldsymbol{E}^{(n)}\right\}$ are the nth derivatives of the electric field with respect to the direction of the tip motion (in this case the z-direction).

When using a lock-in amplifier and using the mth harmonic as reference input, the measured signal s_m is mainly proportional to the mth derivative (+ some addition of higher harmonics) of the electric field at the apex of the tip. When moving the tip with an amplitude of 20 nm in a Gaussian focus with a diameter of 8 µm, the changes of the electric field at the tip's edges are rather linear. This changes when there is a field enhancement between the tip and the sample. As shown in section 2.2, the electric near-field between the apex of the tip and the substrate increases exponentially with the decreasing distance between the tip and the sample. The background signal depending linearly on the tip position is suppressed by detecting at higher harmonics of the tip vibration frequency while the strongly non-linear tip-sample signal is still detectable.

The calculation assumes a perfectly harmonic tip vibration. When the setpoint (that is the ratio of surface engaged to free space cantilever oscillation amplitude) of the AFM is chosen too low, this assumption is not true any more. It was shown that these mechanical anharmonicities can be mistaken for non-linear contributions generated by the near-field [3]. Keeping the setpoint above $\approx 90\%$ of of the free space amplitude ensures harmonic cantilever motion and thus obtaining only optical information.

The probing with a sub-wavelength scale AFM-tip explains the ability of an aSNOM to obtain images of a high resolution. The interaction between the tip and the surface described by the dipole model makes it possible to distinguish between the light scattered in a small vicinity of the tip apex and the light scattered at the tip body even in the far-field. Finally, the lock-in detection at higher harmonics suppresses the parasitic signal and makes it possible to measure the near-field information.

3 Design of the Infrared Apertureless Scanning Near-Field Optical Microscope

The IR-aSNOM can be divided into three separate but interconnected systems: the mechanical setup (described in section 3.4), the optical setup (described in sections 3.1 and 3.2) and the electronic setup (described in section 3.3). Figure 3.1 shows the three parts and how they are connected.

The mechanical setup mainly consists of an AFM with its cantilever vibration (Ω) measured by a deflected laser beam. The IR-aSNOM is a scanning probe microscope (SPM) but in contrast to other SPMs, the tip is held fixed at the position of the focus of the laser beam. Instead of moving the tip itself, the sample is moved underneath it with the help of a sample stage (S). Another mechanical component is the piezo-driven retro-reflector (PA) (shown in the optical setup) to vary the reference path length.

The optical setup consists of the laser source (LS) and a Mach-Zehnder-Interferometer. The light takes a detour to the near-field-optical interaction zone (NFO) at beam splitter BS2. On its way to the NFO and back, the light passes two periscope mirrors (PM) and is then focused onto the tip by a mirror objective (MO) (shown in the mechanical setup). The optical setup shows the possibility of beam preparation (BP). In this thesis, only BP1 is used to parallelize the beam (see section 3.1.2); the other places for beam preparation are not yet used.

The interferometer output beam is detected by an InSb-detector in the electronic setup. The electronic signal is fed into a lock-in amplifier. As reference signal, the nth harmonic of the oscillation frequency of the AFM Ω is passed to the lock-in amplifier. The AFM, the sample stage, the lock-in amplifier and the piezo are all computer-controlled.

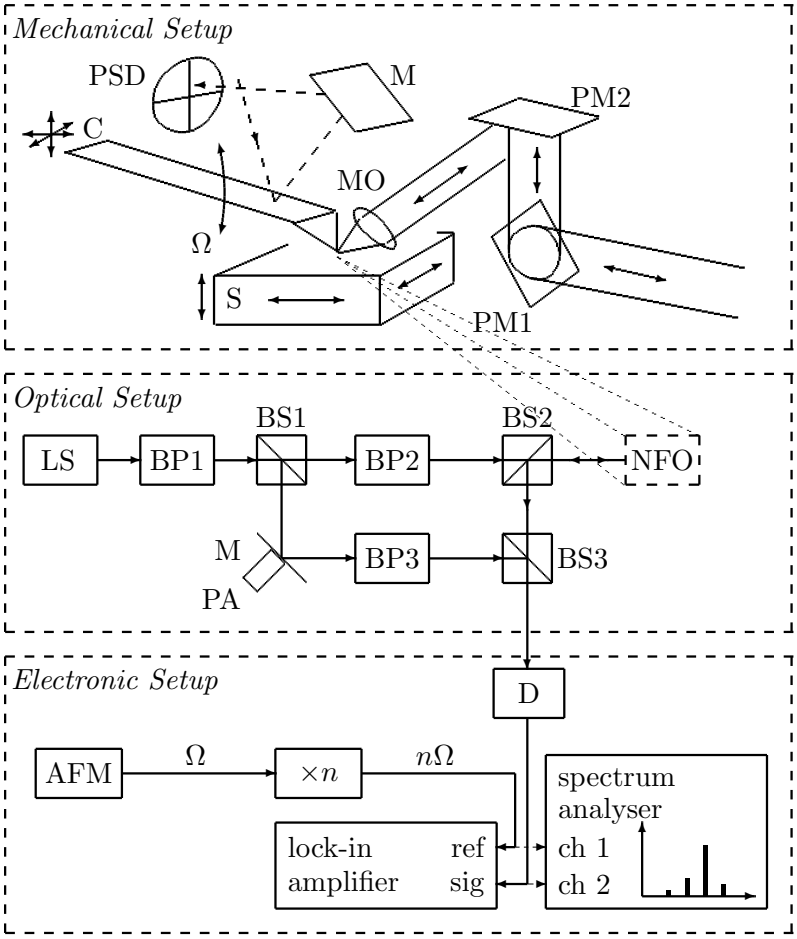

Figure 3.1: Overview of the three major systems of the IR-aSNOM. *Mechanical Setup:* S – sample stage, C – AFM cantilever, M – mirror, PSD – position sensitive detector, Ω – non-contact mode oscillation frequency of the cantilever, PM – periscope mirror, MO – mirror objective. *Optical Setup:* LS – laser source, BS – beam splitter, BP – beam preparation, M – mirror, NFO – near-field-optical interaction region, D – detector, PA – piezo actuator. *Electronic Setup:* Ω – oscillation frequency of the AFM cantilever, n – harmonic index.

3.1 Continuous Wave Infrared Tunable Laser

3.1.1 Continuous Wave Optical Parametric Oscillators

The light source of the IR-aSNOM is a continuous wave optical parametric oscillator (cw OPO), model LINOS OS 4000. OPOs are based on non-linear optics and are able to generate widely tunable radiation in spectral regions inaccessible to traditional lasers [8].

In a linear optical process, the induced polarization $P(t)$ is a linear function of the strength of the applied laser field $E(t)$, $P(t) = \chi^{(1)}E(t)$. Here, $\chi^{(1)}$ is the linear susceptibility[1] describing the linear response of the dielectric material. The induced dipoles oscillate at the same frequency as the optical wave traveling through the material. But in a large optical intensity, the material response becomes non-linear described with the second order susceptibility[2] $\chi^{(2)}$, $P(t) = \chi^{(2)}E(t)E(t)$. In this non-linear optical effect, the dipoles do not only oscillate at the input frequency, but also generate a continuous band of frequencies. Thus, non-linear optical processes can be used to generate new frequencies from an already existing frequency.

Two important non-linear effects for OPOs are optical parametric generation and amplification. The optical parametric generation can be described in the photon picture as the spontaneous break-up of a high-energy pump photon into two constituent parts of lower energy. Because of energy conservation, the sum of the energies of the two new photons is equal to the energy of the pump photon (frequency ω_3). The new photon with the higher energy is usually termed "signal" (ω_2) while the one with the lower energy is designated "idler" (ω_1).

Optical parametric amplification can be viewed as the generation of an electromagnetic wave at the difference-frequency ω_1 of two input frequencies at ω_3 and ω_2 ($\omega_3 > \omega_2$) in a second-order non-linear optical material:

$$\omega_3 - \omega_2 = \omega_1 \tag{3.1}$$

. The process of difference-frequency generation thus automatically leads to amplification of the lower-frequency input field [6].

The strength of this amplification largely depends on the intensity of the input

[1] a tensor of second rank
[2] a tensor of third rank

pump and the signal field. The amplification is strongest, if the phase-matching condition is fulfilled, that is

$$\Delta k = k_3 - k_2 - k_1 \tag{3.2}$$

vanishes. Because of normal dispersion, optical fields at different frequencies normally cannot maintain synchronism over long distances. After traveling a distance l_c (coherence length), the pump, signal, and idler waves suffer a phase difference of π and amplification turns to attenuation. While traveling further, the optical fields slip in and out of phase periodically, and energy is transferred back and forth resulting in no net gain of the signal and idler field.

There are different techniques to achieve phase velocity synchronism. The one used in the OS 4000 is called quasi-phase-matching (QPM) and uses a non-linear material where the orientation of the electric dipoles is periodically reversed by 180° along the pump propagation direction. The result of periodic poling is that the radiated optical waves from the oscillating dipoles in consecutive domains become out of phase by π in both time and space. [8] A poling period (Λ) equal to two coherence lengths preserves a constructive relative phase between the optical fields: $\Lambda = 2l_c$.

The OS 4000 is capable of producing a signal beam with wavelengths ranging from 1.48 to 2.0 µm and an idler beam with wavelengths ranging from 2.3 to 3.8 µm (see [24]). It uses a Nd:YAG laser with up to 2.3 W at 1064 nm as the source for the pump field. As non-linear material, it uses periodically-poled $LiNbO_3$ (PPLN). The PPLN crystal has 35 different poling periods. These poling periods result in 35 different signal wavelengths and idler counterpart wavelengths. A fine tuning of the wavelength in the poling period is done by changing the length of the crystal by variation of the crystal's temperature between 150 and 180 °C. Because the spectra of the poling periods overlap, the OS 4000 continously covers the complete ranges of wavelengths.

To intensify the strength of the pump and the signal field, the crystal is placed in an optical cavity. This principle idea of the OS 4000 is based on the research in the group of Prof. Mlynek (see [34]). The mirrors of the cavity are highly reflective for the pump and the signal beam. The cavity is stabilized by one of the end mirrors, whose position is adjusted to keep the cavity in resonance with the pump frequency by the Pound-Drever-Hall method (see [5]). In this method, the pump

wavelength is varied sinusoidally over a small range with a frequency of 12 MHz. If the cavity is slightly out of resonance, the reflected intensity also varies sinusoidally. If the resonator is too short, the intensity variation is in phase with the variation in frequency, otherwise it is 180° out of phase. One of the resonator end mirrors is mounted on a piezo, and the lock amplifier can keep the resonator back into resonance.

Only signal frequencies in resonance with the cavity and obeying the phase-matching condition can be amplified in the cavity. On some conditions, more than one signal frequency has these properties and the frequency of the signal beam can jump between them. The OS 4000 has two optional etalons to prevent frequency jumping (see [9]). The idler beam is coupled out from the cavity at both sides, while a fraction of the signal beam is coupled out only at one side of the cavity.

3.1.2 Output Beams

With its Gaussian TEM00-output mode and its large continuous tunability, the OPO is a very good continuous wave source. But in practice, there are some difficulties to overcome as discussed here.

Parallelizing the Beam

The OS 4000 uses a single calcium fluoride (CaF_2) lens to couple the beam of the pump laser into the resonator and to parallelize the outgoing signal and idler beams. The waist of the beams at one side of the cavity is in the $\lambda = 1064$ nm focal point of the CaF_2 lens. But this is not the focal point at the signal or idler wavelength. Even with the dielectric constant of CaF_2 being only weakly dependent on the wavelength, the focal length varies by 4.6% from the pump wavelength to the longest idler wavelength (4000 nm). So the radiation emitted by the OS 4000 has its waist not in front of the OPO but behind the collimating lens, and the beam is diverging.

This can be corrected by an assembly of two lenses. In the signal beam, two $f = 50$ mm CaF_2 lenses (Thorlabs: LA5763) parallelize the beam. In the idler beam, one $f = 50$ mm and one $f = 40$ mm (Thorlabs: LA5370) lenses correct the beam and make it smaller.

By sliding the assembly to appropriate locations between the experiment and the laser and by varying the distance between the lenses, it can be assured that the

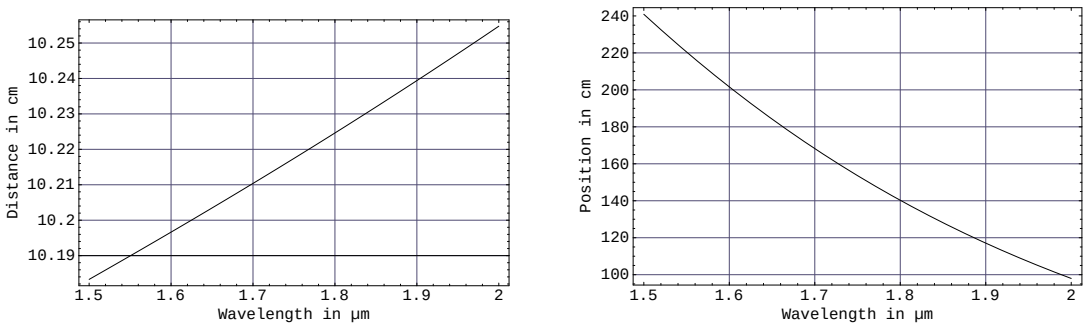

(a) (b)

Figure 3.2: The position and the distance of the two lenses to collimate the signal beam of the OS 4000 for different signal beam wavelengths: (a) the distance between the two lenses, (b) the distance between the first lens and the lens inside the OS 4000.

beam delivered to the experiment always has the same radius. Figures 3.2 and 3.3 show the calculated distance between the lenses and the distance between the lens system and the collimation lens of the OPO. In the calculations, the waist of the beam, the collimation lens of the OPO, and the focal point of the first spherical mirror were kept at fixed positions. The position and the distance of the two lenses were calculated to get a beam waist with a radius of 1.7 mm at the position of the first spherical mirror.

Aligning the Beam

The light of the OPO is too low in frequency to be visible to regular near infrared viewers. These cameras typically work down to a wavelength of about 1 µm. They are not suitable for the alignment of the idler and only partially useful for the highest signal beam energies. Suitable cameras would be certain thermal cameras (which cost more than € 20.000).

For the rough alignment, a standard infrared camera can be used though: the OPO does not only emit the signal and idler light but also reminiscent light from the pump laser (1064 nm) and red light with microwatt power caused by non-phase-matched sumfrequency mixing between the resonant signal and pump waves (see [34]). This light with powers below 1 mW has a different divergence than the signal and idler beams but the same central direction. These reminiscent beams are easily

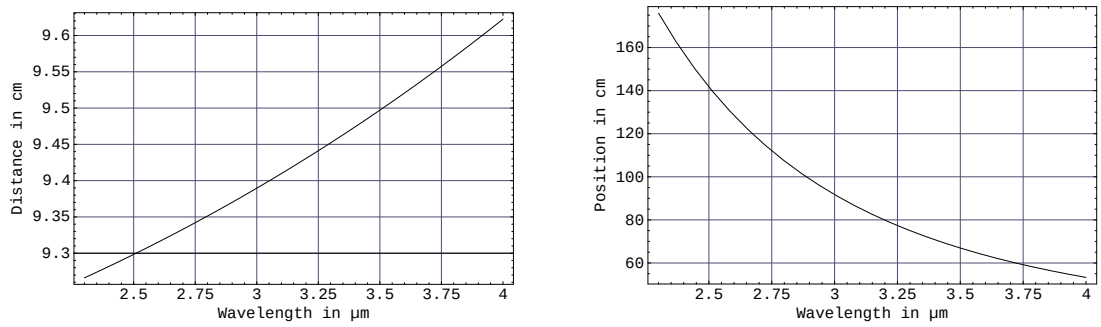

(a) (b)

Figure 3.3: The position and the distance of the two lenses to collimate the idler beam of the OS 4000 for different idler beam wavelengths: (a) the distance between the two lenses, (b) the distance between the first lens and the lens inside the OS 4000.

viewed with a standard video camera and can be used to indirectly do the rough alignment of the collinear signal and idler beams.

For the precise alignment of the signal and idler beam, scanning them with an IR-sensitive detector is helpful. For this approach, we used a PbSe-detector (Laser Components: BP-48). The detector is mounted on linear translation stages (Newport: M-423 and M-433) and moved across the beam. The stages are attached to computer-controlled stepper motors (Physik Instrumente: C-560).

3.1.3 Laser Cavity

The OS 4000 has two laser cavities and each has its own challenges. In the cavity of the pump laser, there are relaxation oscillations that produce intensity noise. While this small amount of noise is not important for most applications of the laser, it turns out to be a problem for the IR-aSNOM. The PPLN crystal is placed in an external cavity. For this cavity, even a small amount of back-coupled light turns out to be a problem.

Prevent Back-Coupling into the Laser Cavity

The first setup of the IR-aSNOM, shown schematicly in figure 3.10(a), realized the standard Mach-Zehnder-interferometer with just two beam splitters. If the setup is perfectly aligned, this results into about 25% of the light being reflected back into

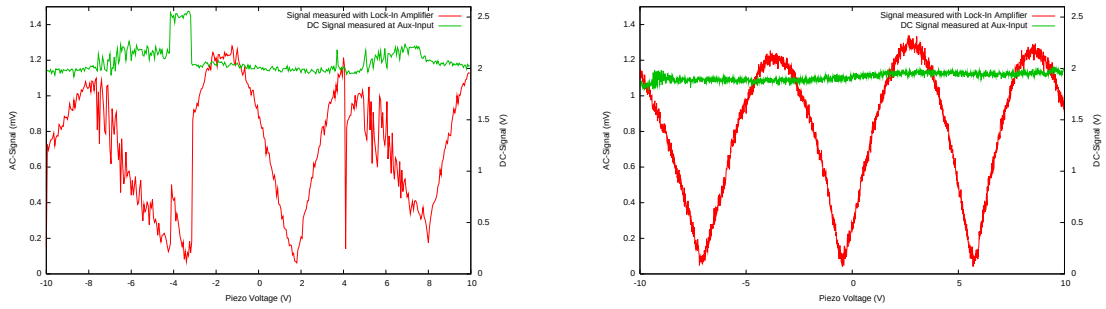

(a) (b)

Figure 3.4: The effect of back-coupling on interferometric amplification. The two graphs show the signal detected by the lock-in amplifier depending on the position of the retro-reflector. (a) shows the effect of back-coupling, (b) shows the same plot when back-coupling is prevented by an iris.

the direction of the laser source. But even a small fraction of the laser light has a big impact on laser stability when reflected back into the cavity.

In most of the poling periods of the OPO, the gain profile of the optical parametric amplification is broad enough to support more than one frequency mode. In normal operation, one of the modes dominates the others. In the first poling periods, one or even two intracavity etalons help to prevent mode hopping.

In the case of back-coupled light, the built-up equilibrium is disturbed all the time, and a very frequent mode hopping is the result. This disturbs the IR-aSNOM with a phase difference instability between the light in the reference and signal path of the IR-aSNOM (not to be confused with the signal beam of the laser). Consequently, the laser looses power stability.

Figure 3.4 shows the impact of back-coupling on interferometric amplification. It shows two graphs where the signal measured with the lock-in amplifier (red) and the DC level at the detector (green) are recorded against the length of the reference path. During the scan, the phase difference between the light coming back from the tip and the reference beam should vary sinusoidally between constructive and destructive interference (see section 2.3). The signal measured with the lock-in amplifier should show the absolute of a sine function as observed in figure 3.4(b). In figure (a), however, one sees the effect of back-coupling. During some periods, the signal has the sine magnitude shape, during other periods, the signal is weaker than it should be. During the same periods, a power instability is observed on the

DC signal of the detector (green graph).

These graphs where taken when the setup shown in figure 3.10(a) was disaligned on purpose. The first beamspitter was tilted so that the reference beam reached the second beam splitter too low for back-coupling. By tilting one of the mirrors of the retro-reflector, the reference beam was directed into the detector. The back-reflected fractions of the illumination beam and the reference beam left the setup with an angle. In figure 3.4(a), a small fraction of the back-reflected beam still reached the laser cavity, in figure (b), the back-reflected light was stopped by an iris. This method stops the back-coupling into the cavity but at the same time, the signal path and the reference path have a slight angle at the detector. This angle reduces the interferometric visibility between the beams and the interferometric amplification.

A Faraday-Insulator between the laser and the setup would prevent the back-coupling. Because there are no off-the-shelf Faraday-Insulators for such a broad wavelength range in the near and mid-infrared, another way of dealing with the problem had to be found. As it can be seen in section 3.5.1, the IR-aSNOM is now built with three beam splitters and no back-coupling occurs anymore.

730 kHz Noise from the Pump Laser

When illuminating a detector with the output from the OS 4000 and connecting the amplifier to a spectrum analyzer, one obtains the spectral distribution of the intensity noise of the laser beam. The blue graph in figure 3.5(a) shows that the noise is not uniformly distributed. From 100 kHz to about 500 kHz the noise level is above the noise level of the system of detector, amplifier and spectrum analyzer (red graph). Between 500 kHz and 900 kHz, the graph shows a high noise level in the shape of a resonance peak. From 2 MHz on, the noise level drops down almost to the noise level of the detection system.

When comparing the noise of the system with the noise of the pump laser (Mephisto 1200: InnoLight) in figure 3.5(b), it is obvious that the noise originally comes from an intensity noise of the pump laser. InnoLight cites relaxation oscillations as reason for this noise (see [15]).

This can be understood by looking at the rate equations for the population in the gain medium. From the rate equations, one can derive two coupled differential equations that not only have a stationary solution but also damped oscillations as

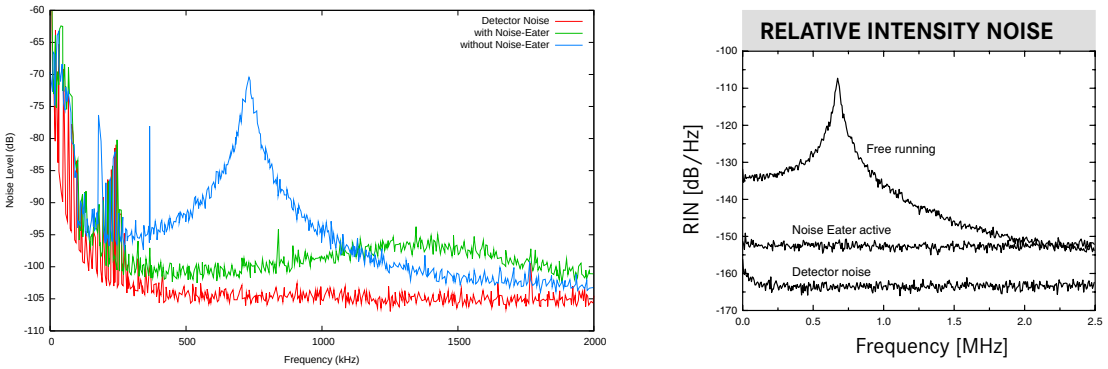

(a) (b)

Figure 3.5: Intensity noise of the laser: (a) Intensity noise spectrum of the OS 4000, (b) Intensity noise spectrum of the pump laser [16].

solution (see reference [9]):

$$\frac{\mathrm{d}^2 n}{\mathrm{d}t^2} + 2\delta\frac{\mathrm{d}n}{\mathrm{d}t} + \omega^2 n = 0 \tag{3.3}$$

where n is the deviation of the population of the upper laser level from equilibrium, δ is a damping constant and ω is the relaxation frequency. In a typical Nd:YAG-Laser, δ is smaller than ω, and every deviation from equilibrium leads to damped oscillations.

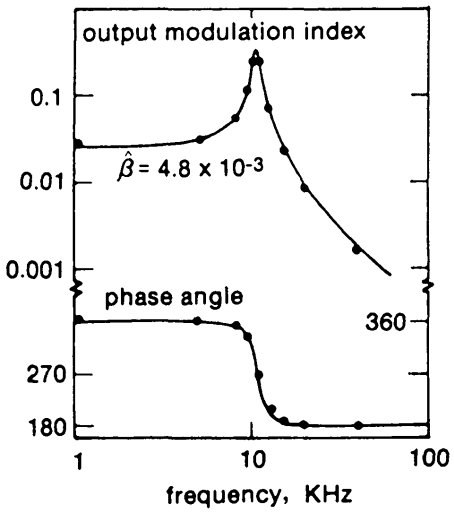

Figure 3.6: Response of a laser to small-amplitude pump modulations (from [35]).

Figure 3.6 shows the spectral response of a laser to small-amplitude pump modulations. The output modulation of the laser power depends largely on the frequency of the pump modulation. This means that noise with a frequency near the relaxation oscillation frequency gets much more amplified than the noise at other frequencies. This noise from the pump laser directly affects the cavity of the OPO and thus is passed on to the light generated by optical parametric amplification. It explains the high noise level at a frequency of about 730 kHz coming from the OS 4000.

The noise can be suppressed by installing an optional "noise eater" InnoLight provides for the Mephisto 1200. The noise eater continuously measures the output power of the Nd:YAG-laser and modulates the input current to keep the power constant. This power modulation of the pump laser is independent of the frequency modulation of the pump laser needed for the Pound-Drever-Hall method to stabilize the resonator (see section 3.1.1). As expected, the noise of the OS 4000 is largely reduced by turning on the noise eater (green graph in figure 3.5(a)).

For the IR-aSNOM, this turns out crucial, because the frequency of the measured signal is near the relaxation oscillation frequency. The resonance frequency of the AFM-tips used in the experiments are at about 250 kHz. To distinguish the nonlinear near-field from the linear background signal, the signal is detected at the third harmonic frequency of the tip frequency, at about 750 kHz. Without the noise eater, the signal at 750 kHz coming back from the experiment is much weaker than the noise of the reference beam used for interferometric amplification. Narrowing the detection bandwidth of the lock-in amplifier would help but would also increase the detection time.

Susceptibility to Vibration Shocks

The OPO is highly sensitive to vibration. Every mechanical shock to the optical table brings the piezo-driven cavity of the OPO out of lock condition for a short moment. In practice, these shocks range from dropping a screwdriver from a small distance onto the table to the vibration of a running stepper motor. For the measurements it is important to adjust the lock amplifier of the OPO properly and to avoid any shocks to the optical table.

3.2 Other Optical Components

After some modifications to the laser itself and to the output beam, the laser is now delivering a parallel beam with only a small amount of parasitic noise. In the next section, I describe the other optical components needed to build the IR-aSNOM. During the search for components, we realized that it is rather difficult to find optical components for the spectral range of the OS 4000. Components that are standard in the visible and the near-infrared range sometimes have to be custom-made for the mid-infrared range of the OPO.

3.2.1 Fiber Optics

We considered the option of delivering the laser beam to the aSNOM by a fiber optic delivery system. A feasible fiber would be a single mode fiber made of Chalcognide InfraRed (CIR) glass and the input and output coupling devices would have to be made of aspheric CaF_2 lenses to ensure efficient focussing into the ≈ 10 µm fiber core. Due to the lack of off-the-shelf products on the market, everything would have to be custom-made. Institut national d'optique (INO) in Québec quoted a price of $CND 28,200 to build such a fiber delivery system. Therefore, we decided to deliver the laser beam with mirrors.

3.2.2 Focusing Objective

To focus the light onto the tip, a lens or an objective with a large numerical aperture (NA) would be preferable. A focussing lens with a large NA gives a small focus spot. It illuminates smaller parts of the tip's body and thus reduces the parasitic backscattered light. At the same time, it collects the scattered light from a larger solid angle and increases the detected signal. The used AFM (see section 3.4.1) was specially chosen to have good access to the tip region. With this instrument, we are limited to an NA of about 0.3 because of geometric reasons.

On the other hand, spherical lenses with a large NA suffer from spherical abberation. The focus size of a spherical lens with an NA of 0.3 is much larger than it could be according to Gauss optics.

Normal glass lenses for the visible spectrum are only transparent up to a wavelength of about 2 µm. To cover the whole spectral range of the OS 4000, the used

lenses have to be made of special glasses like CaF_2, MgF_2 or Sapphire. I tried to get an aspheric CaF_2 lens as focussing lens but didn't find a producer of such lenses.

In the end, I decided to take the ×15 reflecting objective NA 0.28 (25-0506) from Ealing Catalog. In this objective, three of the primary monochromatic aberrations are corrected: the primary spherical aberration, coma and astigmatism[3]. This objective is expected to produce spot sizes between 6.6 µm ($\lambda = 1.5$ µm) and 17.4 µm ($\lambda = 4.0$ µm). Besides the corrected spherical aberration, the mirror objective is also achromatic. It has the same focal length for all wavelengths.

The objective was ordered with a protected silver coating (25-0506-99) because silver has an even better reflectivity in the near and mid-infrared than a gold coating. It also has a reflectivity of more than 90% at a wavelength of 400 nm (see figure 3.7). Gold has this reflectivity only down to 600 nm. Therefore, with the silver coating we are able to use the objective in the visible spectrum as well.

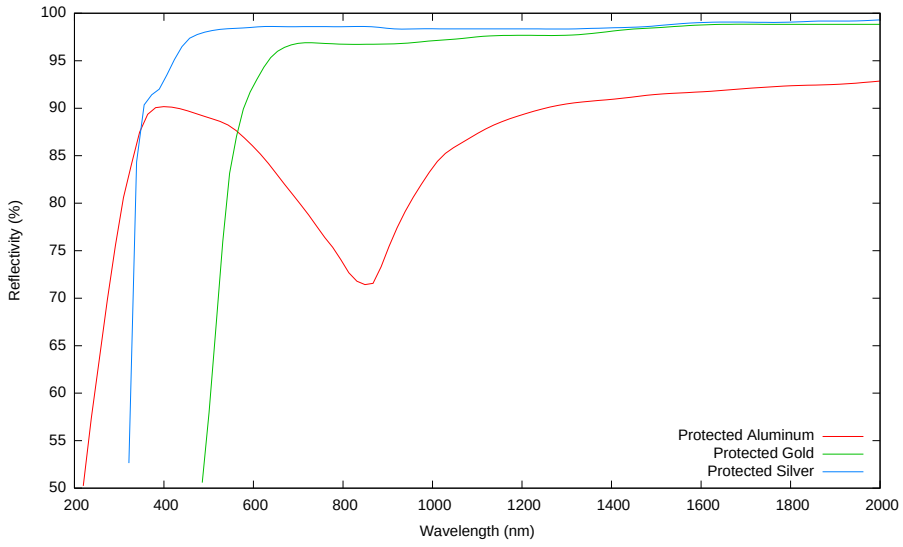

Figure 3.7: Comparison of the reflectivity of different protected metal coatings [39]. Protected silver is the best choice for the IR-aSNOM.

3.2.3 Beam Splitters

In the IR-aSNOM, zinc selenide (ZnSe) windows are used as beam splitters. They are broad band antireflection (BBAR) coated on one side for the wavelengths from

[3]Primary aberrations are those that can be described by third-order theory (see [20, page 142]).

1.5 µm to 4.0 µm and an angle of incidence of 45° on the back to reduce ghost images. They were custom-made by Lambda Research Optics (BBAR1-WI-2503Z-1.5-4.0-45).

At the uncoated surface of the ZnSe window, 30% of the s- and 8% of the p-polarized light is reflected. At the BBAR-coated side of the window, at maximum about 5% of the s- and 0.5% of the p-polarized light is reflected.

At first, it might seem to be a disadvantage that the beam splitters do not split the power evenly. Given sufficient input power, though, it is actually an advantage to use beam splitters with a higher transmission than reflectance. Less of the signal carrying backscattered light from the sample gets lost, while the input power, which is delivered by reflectance, can be increased to the desired level.

3.2.4 Mirrors

The reason for choosing the protected silver coating is the same as for the reflecting objective (see section 3.2.2).

For flat mirrors, $\lambda/10$ protected silver mirrors from Thorlabs were taken. We chose 1/2" (PF05-03-P01) as size of the mirrors to guide the laser to the setup and for the periscope. 1/2" fits a 7 mm beam diameter. For convenience, we chose larger 1" mirrors (PF10-03-P01) for the retro-reflector and in the interferometer.

Instead of using lenses to expand or focus the beam, spherical mirrors were taken, because the focal length of focussing mirrors is not wavelength-dependent. So the optical elements do not have to be readjusted with every change of the wavelength.

We use spherical mirrors from Edmund Optics and Thorlabs: mirrors with $f = 76.2$ mm (Edmund: L43-342) and $f = 150$ mm (Thorlabs: CM508-150-G01) to expand the beam from the laser and mirrors with $f = 508$ mm (Edmund: L32-821) to focus the beam into the detector.

As mounts for mirrors and beam splitters we chose the 1/2" (KS05/M) and 1" (KS1) Ultra Stable Kinematic Mirror Mounts from Thorlabs. These mounts have superior mechanical stability, and their small backlash effect eases the alignment.

3.3 Electronic Components

3.3.1 Detector

The detector has to fulfill a number of requirements. On the one hand, the detector has to be able to detect very weak signals, on the other hand, it has to have a large linear response dynamic range for truthful interferometric amplification. The cantilever frequencies usually lie between 50 kHz and 500 kHz. To be able to detect the third or fourth harmonic of the signal, the detector has to have a bandwidth well above 2 MHz.

In the infrared, one often uses mercury cadmium telluride (MCT) detectors. Photoconductive (PC) MCT-detectors are normally slower in frequency response than photovoltaic (PV) detectors but the photoconductive detectors, do have a larger linear response regime.

It turns out that for the IR-aSNOM indium antimonide (InSb) photovoltaic detectors are the best choice. They have a better linearity characteristic and have a lower rise time than PV MCT detectors. The InSb-detector from InfraRed Associates (IS-0.5) used in the IR-aSNOM has an active area of $0.5 \times 0.5\,\mathrm{mm}^2$ and is liquid nitrogen cooled. With its peak sensitivity wavelength λ_{Peak} being at 5.1 µm, it can be used in the spectral region between 1 µm and 5 µm. The detectivity at its peak wavelength D*(λ_{Peak},1000 Hz) is $3.26 \cdot 10^{11}$ cm$\sqrt{\mathrm{Hz}}$/W. At a wavelength of 4.0 µm and with a lock-in bandwidth of 1000 Hz, the noise-equivalent power (NEP) of the detector is 6.5 pW. The response of the detector is 3.50 A/W. InfraRed Associates assures that the non-linear response regime starts above 2.5 mW. Together with a specially fitted amplifier, the detector has a bandwidth (−3 dB) from DC to 5 MHz.

3.3.2 Amplifier

To amplify the signal from the detector, we use a current amplifier from FEMTO (HCA-S). The amplifier is custom-built and is similar to the HCA-4M-500K-C current amplifier but with a transimpedance amplification of only $5 \cdot 10^3$ V/A. This was necessary to avoid the strong DC component in the signal to drive the amplifier into saturation. The input noise of the amplifier is 2 pA/$\sqrt{\mathrm{Hz}}$.

3.3.3 Expected Detector/Amplifier Performance

The aim of the detector is, with the help of interferometric amplification, to detect signal levels below 0.1 pW, a typical optical power of the signal. The typical power of the reference beam is 0.1 mW. By equation 2.11 we calculate an interferometric amplified signal strength of 6.32 nW. With the system of detector (3.50 A/W) and amplifier ($5 \cdot 10^3$ V/A), this results in an electric signal of 110 µV on top of a DC voltage of 1.75 V.

There are different components that contribute to the noise of the detected signal: the noise of the detector, the input noise of the amplifier, and the input noise of the lock-in amplifier. But all these noises are negligible compared to the shot noise, which is due to the strong DC signal and the fact that the photo current is carried by discrete particles. It is calculated as:

$$I_{\text{shot noise}} = \sqrt{2 * e * I * \Delta f} \tag{3.4}$$

where e is the elementary charge, I is the current, and Δf is the bandwidth. Taking a lock-in bandwidth of 1000 Hz, the shot noise gives a noise level of 1.67 µV. This would still mean a signal to noise ratio (SNR) of about 66:1.

3.3.4 Lock-In Amplifier

The electronic signal from the amplifier is fed into a lock-in amplifier (Stanford Research: SR844).

The AFM vibration signal is used as lock-in reference signal. In $1f$-mode, the signal is taken directly from the controller box of the AFM. The SR844 offers a special mode for $2f$ harmonic detection. For $3f$ operation, we use an overdriven amplifier to create higher harmonics. Before using the output as reference signal, a 6th order Butterworth band-pass filter is used to suppress all other harmonic components of the signal.

3.4 Mechanical Components

To ensure a stable optical alignment the setup is placed on a standard vibration damped optical table. Furthermore the interferometer is placed on a low thermal

expansion bench plate. Like the mirror holders all mechanical components have to fulfill stability criteria to ensure a reproducible and steady alignment. Other mechanical components, for example the periscope, are needed because of the geometric restrictions of the atomic force microscope (AFM).

3.4.1 Atomic Force Microscope

The AFM used in an aSNOM should have a convenient access to the tip region. The IR-aSNOM uses the M5 from Veeco (formerly Park Scientific Instruments) which has enough space to access the tip from the side with an objective. The 100 µm scanner head offers a travel range of more than 100 µm in the x and y direction. This travel range is used to scan for the focus with the AFM (see section 4.1). For the larger focus size of the infrared beam the travel range should not be smaller than 100 µm. In the z-direction, the AFM has a piezo travel range of 6 µm. In addition, the head has a stepper motor for coarse motion in z-direction.

The AFM is equipped with an imaging camera unit for monitoring the top of the sample. To measure the vibration of the AFM tip, a 670 nm diode laser is focussed on the top of the AFM cantilever and the reflected beam is positioned on a quadrant diode. The deflection signal is used to synthesize the reference signal for the lock-in amplifier as well as to measure the vibration amplitude.

As described in [4], the shape of the AFM tip is important for an aSNOM. When the beam is focused onto the tip apex, the tip body should be illuminated as little as possible. For the IR-aSNOM we use AdvancedTEC Non Contact (ATEC-NC) tips from Nanosensors. Figure 4.1 shows a side view of the tip. The tips are made of Si and have a natural SiO_2 layer at the outside. To get a larger local field enhancement in some measurements, we may metal-coat the tips with a coating such as 20 nm of Pt/Ir.

3.4.2 Nanopositioning Stage

The scanning area of the AFM is used to position the tip in the focus. To keep the tip always in the same spot of the focus, it is best to scan the sample below the tip and to keep the tip at the same spot where it was (see [2]). For this purpose, a digitally controlled 3-axis piezo scanner stage (Physik Instrumente: P-517.3CD

scanner, Physik Instrumente: E-710.3CD controller) is positioned below the AFM. The travel range of the piezo stage is 100 µm in the x- and y-direction and 20 µm in the z-direction. The scanner stage is equipped with capacitive sensors and is able to position the sample with a precision of 1 nm in x- and y-direction. In z-direction, the precision is even as high as 1 Å.

For the coarse approach in z-direction, there is a miniature dove-prism z-translation stage (Newport: M-DS25-Z) mounted on the nano-stage.

The digital piezo controller has a digital I/O port to control the position with a computer. The same port also delivers a trigger signal used to synchronize the data aquisition of the lock-in amplifier (see section 3.3.4).

3.4.3 Bench Plate

The bench plate was home-made from INVAR 36® (Material-No. 1.3912) to minimize thermal drift effects on the interferometric measurements. Using materials with a low thermal expansion coefficient has shown to improve the performance of the instrument dramatically (see [2, page 63]). INVAR 36® is an alloy of 36% nickel and 64% iron.

3.4.4 Periscope and Translation Stage

To illuminate the tip with the objective, we built a periscope. At an angle of 17° between the axis of the objective and the sample, the beam from the objective is just touching the sample. The periscope was also designed to have the focal point of the objective on a height of 50 mm.

The head of the AFM can be moved 120 µm in the x- and y-direction. This travel range can be used to move the tip into the center of the focus, but the rough focusing onto the tip is done by an x-y-translation stage and the stepper motor of the AFM. The periscope is mounted on a low profile two-axis aluminium translation stage (Standa: 7T273-10T). The translation stage has one of the driving screws rotated by 90° for convenient handling. It has a travel range of 10 mm and a tracking accuracy of 2 µm. The translation stage is fixed onto a kinematic mount to allow for the whole periscope to be removed from the setup to access the AFM head. This has to be done, for example, to change the tip.

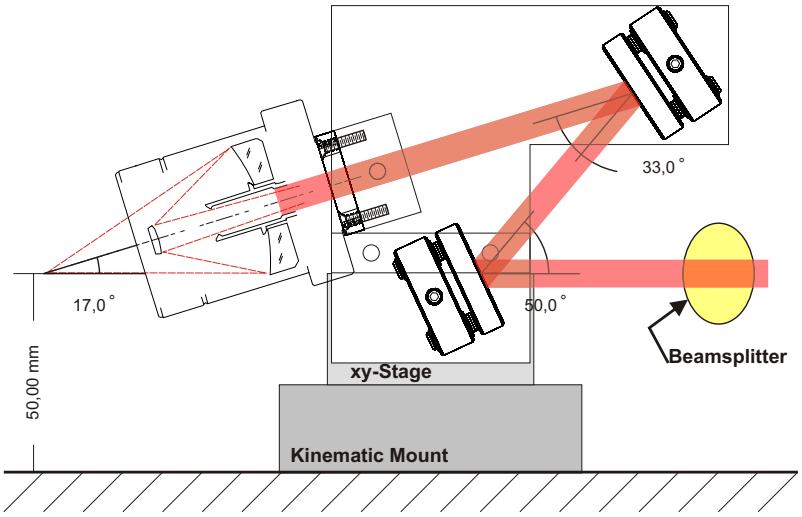

Figure 3.8: Design of the periscope

3.4.5 Retro-Reflector

In homodyne mode, an aSNOM needs to be able to change the length of the path of the reference beam. In the IR-aSNOM, we designed a piezo-driven retro-reflector. The retro-reflector is home-made and uses two narrow cut-outs of thin copper as flat springs. A table is mounted between the two sheets of copper. The piezo actuator (PI Ceramic: PICMA Monolithic Multilayer Piezo Actuator, P-855.51) is pressed against the table by a micrometer screw. On top of the table, we placed two mirror mounts (Thorlabs: KS1) with silver mirrors. The piezo has a nominal displacement of 15 µm between 0 and 100 V. Because we use a voltage between -10 and 10 V from an auxiliary output of our lock-in amplifier, we have a maximal displacement of about 3 µm, resulting in a path elongation of about 6 µm, sufficient to achieve an elongation of $\lambda/4$, with λ being 4 µm at maximum.

3.5 Assembly of the Components

In this last section, I will describe what kind of interferometers could be used for interferometric amplification in the IR-aSNOM. Finally, I will describe how we implemented the most advantageous of these interferometers in a comparatively

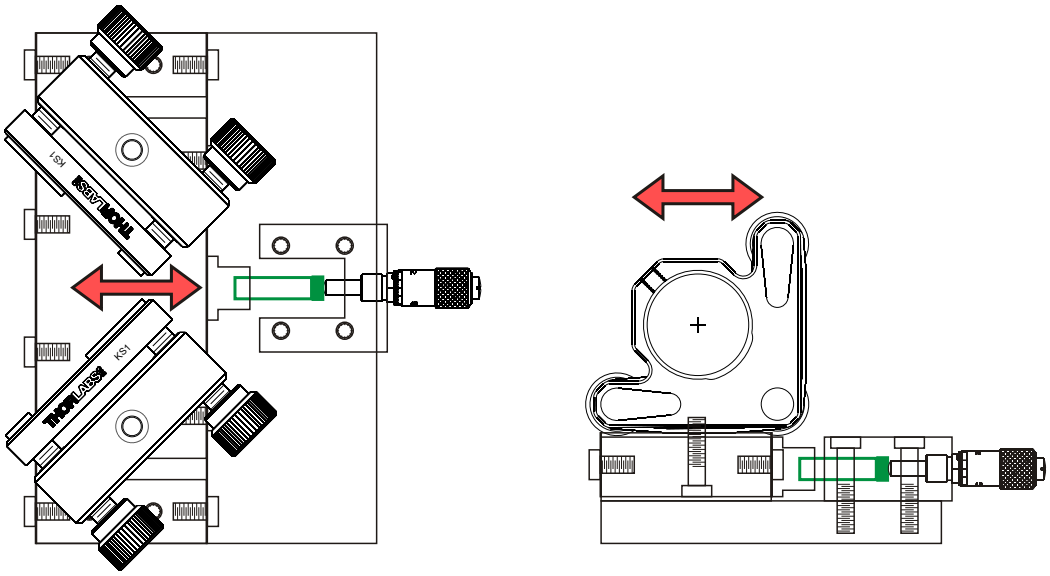

(a) top view (b) side view

Figure 3.9: Design of the retro-reflector: the mirrors can be moved back and forth with a piezo (green)

simple design.

3.5.1 Feasible Interferometer Types

Figure 3.10 shows different types of interferometric setups that could be used in an aSNOM. Each setup has its own advantages and disadvantages.

Setup (a) uses a standard Mach-Zehnder type interferometer. The reference path and the illumination path are separated at beam splitter BS1. The illumination path goes through BS2 to the near-field-optical interaction zone (NFO). On the way back from the NFO, a fraction of the signal beam is reflected at BS2 towards the detector (D). At the same time, BS2 is used to mix the reference beam with the signal path. The advantage of this setup is that the light in the illumination path and reference path can be manipulated separately. For the IR-aSNOM, this setup has a big disadvantage though: about 25% of the light coupled into the setup goes back towards the laser source (LS). In a well aligned setup, some of this light makes its way back into the laser cavity, destabilizing it considerably as described in section 3.1.3.

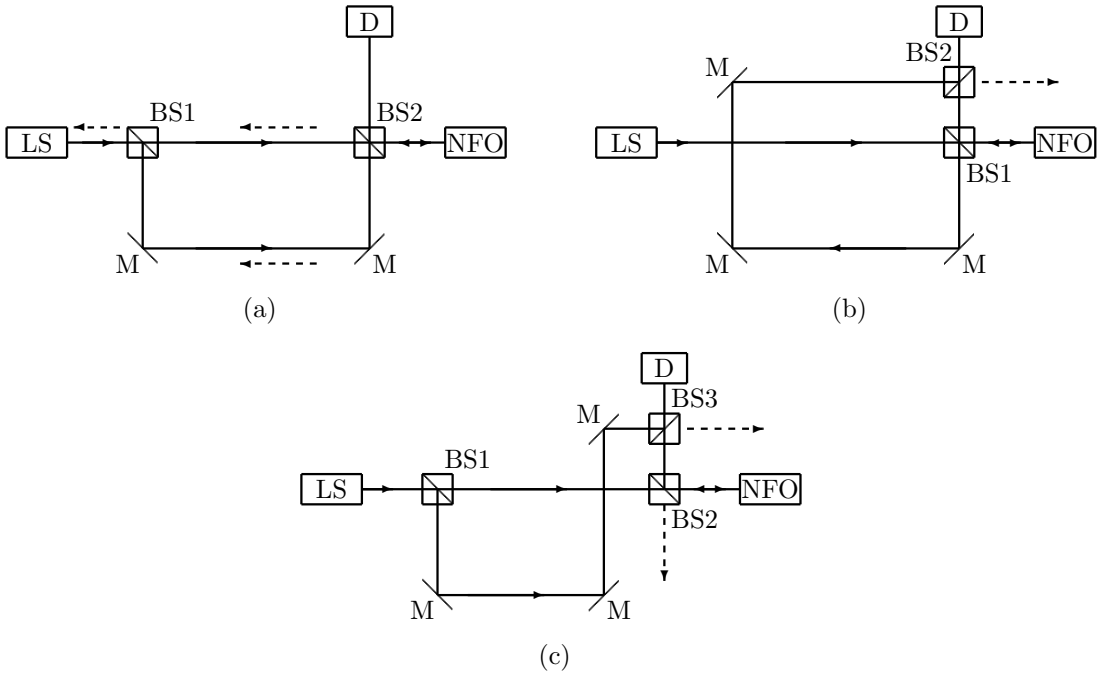

Figure 3.10: Different possible designs of the setup: LS – laser source, BS – beam splitter, NFO – near-field-optical interaction region, D – detector, M – mirror

Setup (b) is more like a Michelson interferometer. Beam splitter BS1 is used to separate the illumination path from the reference path, and at the same time, it is used to reflect a fraction of the signal path to the detector. But unlike in a Michelson interferometer, the reference path is not simply back-reflected but to prevent back-coupling, it is mixed into the signal path at BS2. Only the small amount of light coming back from the NFO is reflected back towards the laser. The big disadvantage of this setup is that the light in the illumination path cannot be manipulated independently from the light in the reference path or the signal path.

The IR-aSNOM uses a combination of these two setups, shown in figure 3.10(c). It is a Mach-Zehnder-like interferometer, such as setup (a), but the reference path is mixed with the signal path at BS3. A small disadvantage of this setup is that the signal coming back from the NFO has to pass two beam splitters to reach the detector, and an additional 30% of the signal is lost. On the other hand, the beam splitters in the IR-aSNOM are chosen to be more transmitting than reflecting (see section 3.2.3), and the setup can be set up in such a way that the signal is transmitted

through the two beam splitters. In the actual setup, still more than 35% of the light in the signal path is transmitted to the detector (considering s-polarized light and the combined effects of *all* mirrors, beam splitters and the obscuration of the mirror objective).

3.5.2 Implementation of the Design

Figure 3.11 shows an overview of the setup. The laser light is delivered from the right. Before it reaches the setup, it is parallelized by two lenses (see section 3.1.2). On the INVAR plate, the beam gets expanded by two spherical mirrors. At the first beam splitter, the beam is split into the reference path and the illumination path. The reference beam reaches the third beam splitter by the retro-reflector. The illumination beam reaches the periscope by being reflected at the second beam splitter. The leftover beams of the illumination beam and the reference beam are blocked afterwards or can be used for alignment. The reflected illumination beam is directed into the periscope. The two mirrors on the periscope (see figure 3.8) direct the beam into the mirror objective, and the beam is focused onto the AFM-tip. The backscattered light from the tip gets parallelized by the objective and is directed back to the second beam splitter by the two mirrors on the periscope. The signal path has to pass the beam splitter BS2 and is then mixed with the light of the reference arm in BS3. This interferometer output path is then focused by a spherical mirror onto the detector.

The amplifier is placed near the detector to minimize the pickup noise between the detector and the amplifier. The nanopositioning stage which holds the sample is placed underneath the AFM head. It facilitates the raster scanning of the sample without moving the AFM tip.

Figure 3.12 shows a photograph of the implementation. The picture shows all parts of the IR-aSNOM except from the nanopositioning stage and the mirror objective which are hidden by the periscope. It also shows the plexiglass isolation enclosure around the setup which isolates the setup from air convection and sound waves and has proven to improve the stability of the interferometer [2].

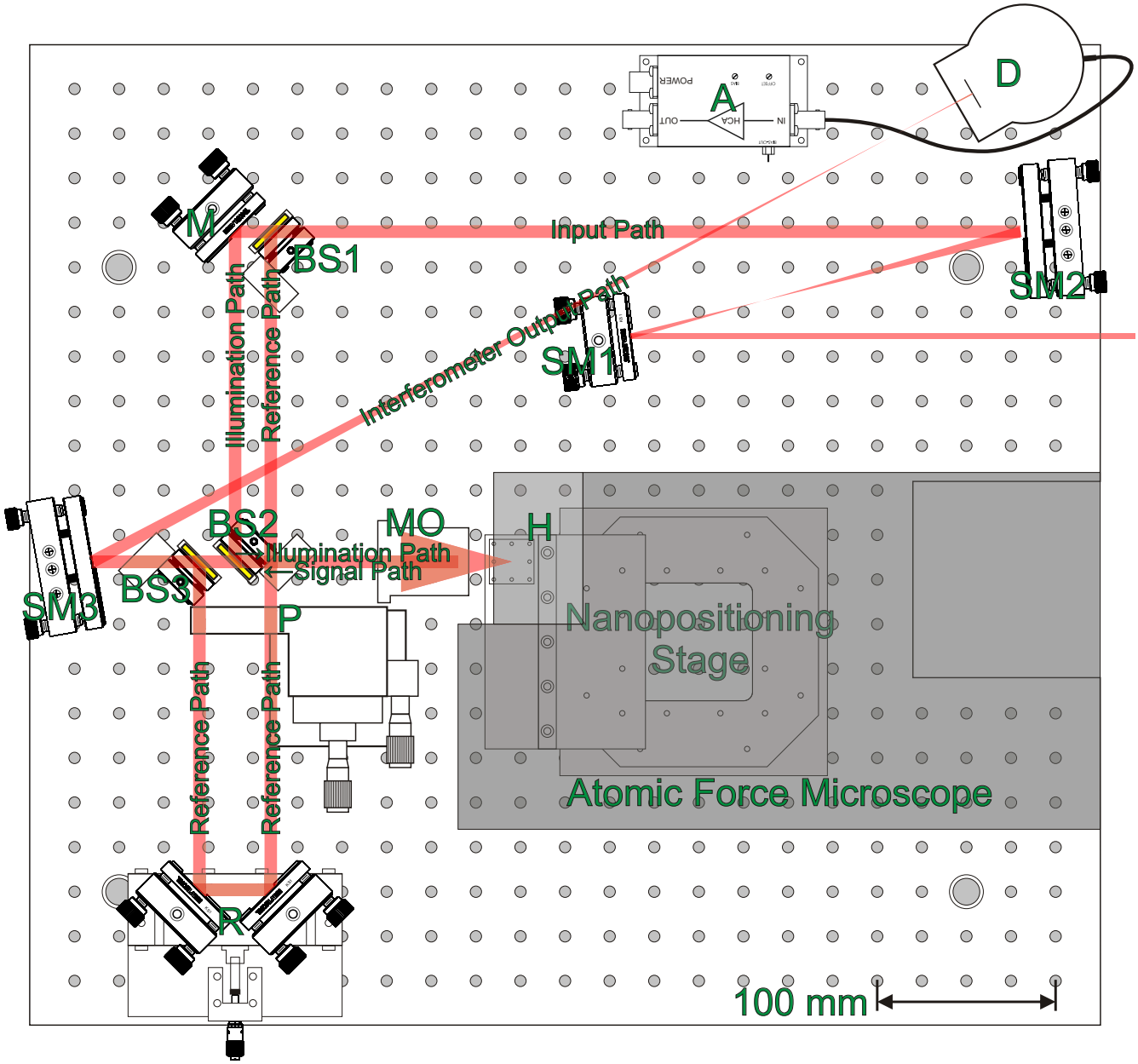

Figure 3.11: Top view of the Setup of the IR-aSNOM: SM – spherical mirror, BS – beam splitter, M – mirror, R – reflector, P – periscope, MO – mirror objective, H – AFM-head, D – detector, A – amplifier

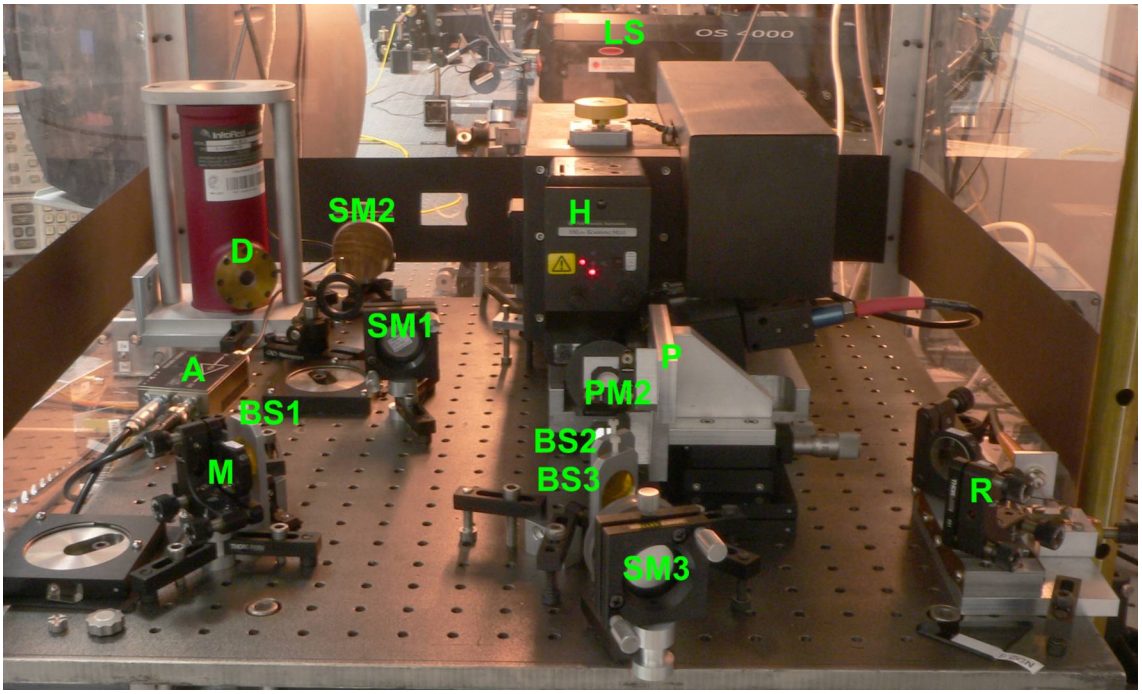

Figure 3.12: Photo of the setup: LS – laser source, SM – spherical mirror, BS – beam splitter, M – mirror, P – periscope, PM – periscope mirror, R – retro-reflector, H – AFM-head, D – detector, A – amplifier.

4 Performance Tests

Before being able to take images with the IR-aSNOM, different aspects of the instrument have to be checked. In this chapter, I will explain how the alignment of the setup is done, how the stability of the interferometric amplification is checked and how to verify that the instrument is indeed capable of detecting near-fields as predicted by the dipole model.

4.1 Alignment

A good alignment of the optical components of the setup described in chapter 3 is fundamental to operate the IR-aSNOM. The tip apex has to be positioned in the middle of the focus of the laser beam with sub-wavelength accuracy, and the backscattered light has to be focused onto the detector. These two tasks are not trivial with a visible laser beam and even harder with an invisible infrared beam.

To get a good alignment, the fact was used that the setup of the IR-aSNOM is achromatic. A HeNe-laser helped to do the coarse alignment of the setup. The shadow of tip in the focused red laser beam is used to position the tip in the focus, and the backscattered light is used to align the detector. In the next step, with the help of the beam-scanning method described in section 3.1.2, the infrared beam is aligned to be collinear to the visible laser. Because collinearity can only be achieved within certain limits, the focus does not stay at exactly the same point. Nevertheless, with this method the tip can be positioned within a range of 40 µm to the actual infrared focus.

The precise positioning of the tip now has to happen electronically. For this we use the scanning area of the AFM. We do a scan with a large tip amplitude ($\approx$ 500 nm) and no sample underneath, and instead of recording the topography, the AFM records the output of the lock-in amplifier. When the vibrating tip is in the focused beam, it varies the intensity of the backscattered light. The lock-in is used

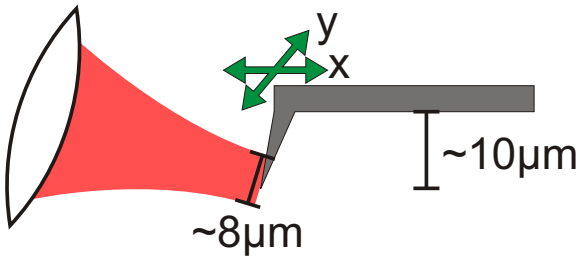

Figure 4.1: Using the tip to scan through the beam in x-y-direction.

with a small time constant (1 ms) and in first harmonic mode. The backscattered light is strong enough so that no interferometric amplification is necessary. These scans (one example is shown in figure 4.2(a)) give an idea of the size of the focus, and by taking images at different heights, it is possible to position the tip in the focus of the beam.

This method is more complicated in the IR-aSNOM than in an aSNOM with visible excitation. Unlike with a visible laser, it is not possible to see from which part of the tip the light is scattered back. As shown in figure 4.1, the focus diameter is in the range of the tip height. The backscattered light does not only originate from the tip apex, which makes it harder to interpret the focus scans.

Another possibility to find the focus is to scan directly for the near-field signal. This can be done by scanning with a small amplitude while in contact with the sample. Figure 4.2(b) shows that there is only a small region of the sample giving a signal when detecting in third harmonic mode.

4.2 Interferometric Amplification Check

The next thing checked is the performance of the retro-reflector. We positioned the tip in the focus, mixed in the reference beam and recorded the signal with the lock-in in first harmonic mode while varying the reference path by sweeping the voltage at the piezo from -10 to $+10$ V. As it can be seen in figure 3.4(b), these plots show the sine absolute behavior expected from equation 2.9.

Possible problems that we ruled out by taking piezo scans were drift problems, such as thermally drift. Drifts in the order of $\lambda/10$ per time to scan one line with the IR-aSNOM ($\approx 1 - 4$ s) would have caused serious problems. Taking the data for

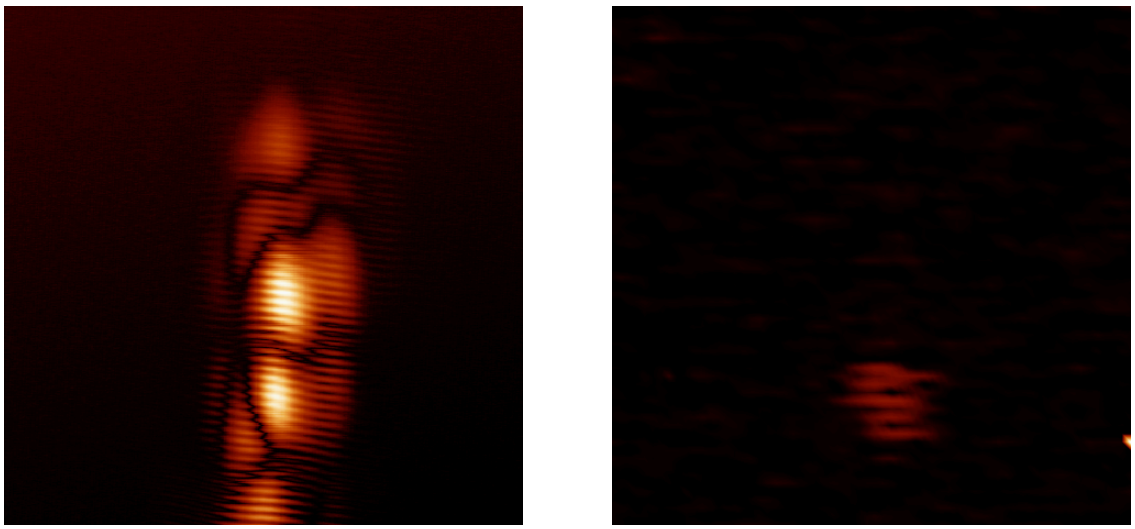

(a) (b)

Figure 4.2: Scanning the beam with the tip gives an idea of the focus size and the spot with the maximum intensity. (a) shows a 80×80 µm scan taken with a large amplitude and detection in first harmonic mode without interferometric amplification. (b) shows a 60×60 µm scan taken while in contact with the sample. The vibration amplitude is about 20 nm and the signal is detected in third harmonic with interferometric amplification.

the shown graph took more than 3.5 min, corresponding to a path length variation of roughly $\lambda/100$ per second. Drift effects would have been clearly visible in the piezo scans. With the path length changes between reference and signal path due to drift being small enough for SPM operation of the IR-aSNOM, we can do a whole line-scan, change the length of the reference path and do a second line-scan. We routinely take reflector scans to calibrate ΔV to change the reference path length by $\lambda/4$.

4.3 Nearfield Verification

Verifying that one is measuring near-field signal with an aSNOM is often done by taking approach curves. Figure 2.3 shows a static approach curve. It shows that the backscattered light from the tip-sample system rises non-linearly in the last 20 nm before reaching the surface. Taking approach curves in the experiment is done with

the lock-in working in second or third harmonic to suppress background scattering. When the tip apex is entering the non-linear region of the static approach curve, the signal at the lock-in suddenly gets stronger.

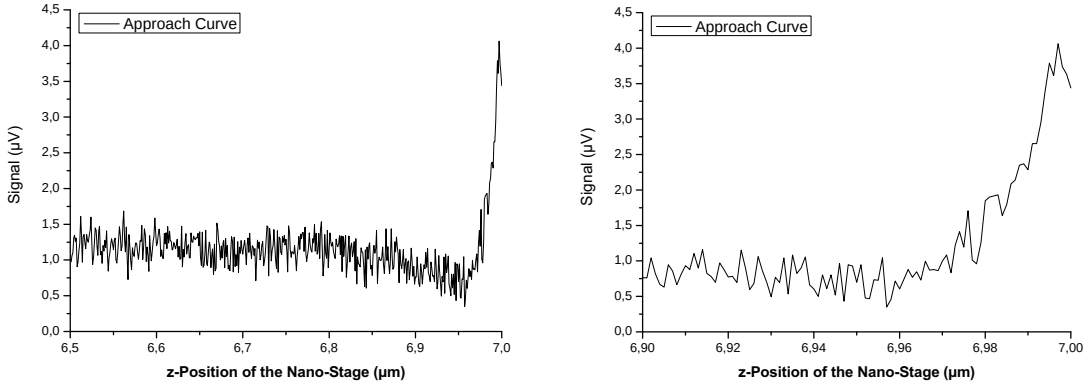

(a) (b)

Figure 4.3: The signal of a Pt/Ir-coated tip approaching a gold surface. The vibration amplitude of the tip was 38 nm. The lock-in amplifier was used in third harmonic mode.

Figure 4.3 shows the approach curve of a metallized tip approaching a gold surface detected in the third harmonic. (a) shows that the detected signal stays constant for a long time, and only just before the sample reaches the tip at a vertical location of 7 µm, the signal suddenly rises.

In fact, to prevent the tip from damage, the approach curves were taken the other way round. The tip is in contact with the sample and the feedback loop is opened shortly before the nanostage starts lowering the sample. The AFM software shows that the tip vibration amplitude reaches a constant value when the sample stage is lowered two or three nanometers showing that the tip is not in contact anymore. This can also be seen when zooming into the approach curve (see figure (b)). It shows that the measured signal, while still in contact, is lower than the maximum signal. This may have different reasons and is also observed in approach curves of other aSNOMs, for example [38].

It can also be seen that the signal-to-noise ratio is about 4:1 and thus lower than we expected in section 3.3.3. The reason might be that the original signal is smaller than we expected. We also did not take the obscuration of the mirror objective and the losses of the mirrors and the beam splitters into account. All these losses add up

so that the signal that reaches the detector is only about 35% of the original signal. The loss of power at the window of the detector also has to be taken into account. In the calculation of the expected detector performance, we used the maximum spectral response, and the response at a wavelength of $\lambda = 2.50$ µm is only about 30% of this response. These factors explain the low signal to some extent but not completely.

5 First Applications

Having built the IR-aSNOM and having checked the performance of the components, I performed first experiments to demonstrate the instrument's capability to obtain images with sub-wavelength resolution. The samples used for these investigations were small gold patterns on glass slides and so-called split-ring structures. I obtained optical images from both samples, and the resolution was as high as $\lambda/50$.

5.1 Material Contrast, Lateral Resolution

The IR-aSNOM can be used to obtain material contrast with high spacial resolution. The fact that different tip-samples systems have different effective polarizabilities has already been discussed in section 2.2. The much higher polarizability of a Pt-coated tip over a gold surface shown in figure 2.3 lets us expect a good contrast of gold structures on a glass surface. The sample we used had structures of different sizes, the larger structures were made by optical lithography, the smaller ones by e-beam lithography on a flat glass surface. This kind of sample is useful to test the instrument because it offers the possibility to compare the simultaneously acquired topography and optical signal.

Figure 5.1(a) shows the topography of the scanned area. On the lower right side is the investigated gold structure. The width of the lines forming the structure is about 600 nm. The other bright area on the upper left shows a gold track from one of the larger structures on the sample. The bright spot on the left is indicating a small high object, probably a dirt particle on the sample. Figure 5.1(b) shows the recorded optical signal. In the glass regions, the recorded signal is at the noise level. Over the gold structures, the detected signal is about three times as high.

During the measurement, the tip was vibrating at a frequency of 275 kHz with a (nominal) amplitude of 41 nm, the lock-in amplifier was used in third harmonic

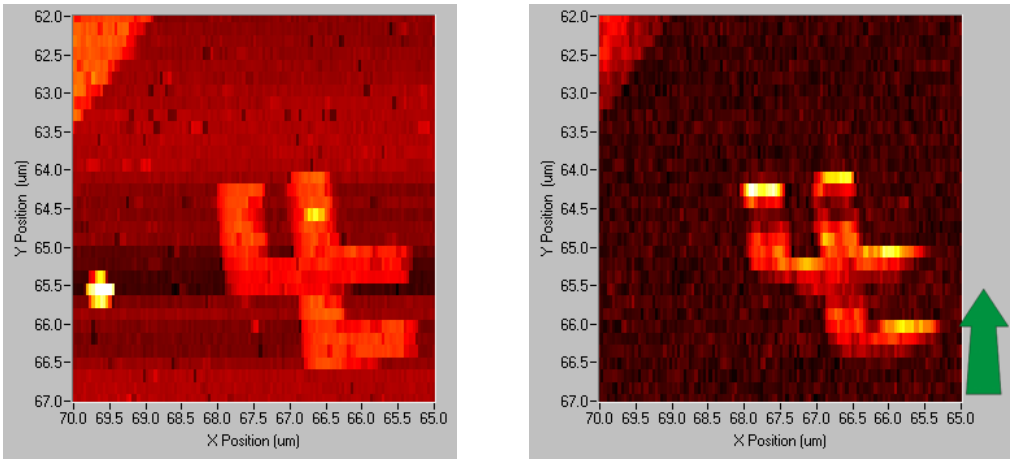

(a) (b)

Figure 5.1: A 5×5 µm scan of a gold pattern on glass. (a) shows the topography. Brighter points indicate higher regions. (b) shows the optical signal s3 obtained in third harmonic mode. The green arrow indicates the direction of the illumination beam which has a wavelength of $\lambda = 2.50$ µm.

mode[1] and the integration time was 10 ms. The data acquisition rate of 32 Hz was carefully chosen to ensure that each measured data point is independent from the last. The laser was tuned to a wavelength of $\lambda = 2.50$ µm, and the power delivered to the experiment was about 40 mW, of which about 3 mW illuminated the tip-sample gap volume.

With the gold structure having a total width of little more than the wavelength, this image already shows that the IR-aSNOM has the capability of measuring with sub-wavelength resolution. Because the dirt particle visible in the topography shows no signal recorded with the lock-in, this image also shows that the obtained information does not originate from mechanical influences.

Figure 5.2(a) shows a zoom of the upper right inner edge of the structure. To determine the resolution of the image, we looked at a line scan along the green line, shown in figure 5.2(b). The two horizontal green lines mark the average optical signal on gold and on glass respectively. We measure the distance in which signal $s3$ falls from gold level to the glass level and estimate a resolution of about 50 nm corresponding to $\lambda/50$. But as the signal on the gold pattern is not homogeneous, it is hard to measure the resolution.

[1]The signal measured in third harmonic mode is called $s3$.

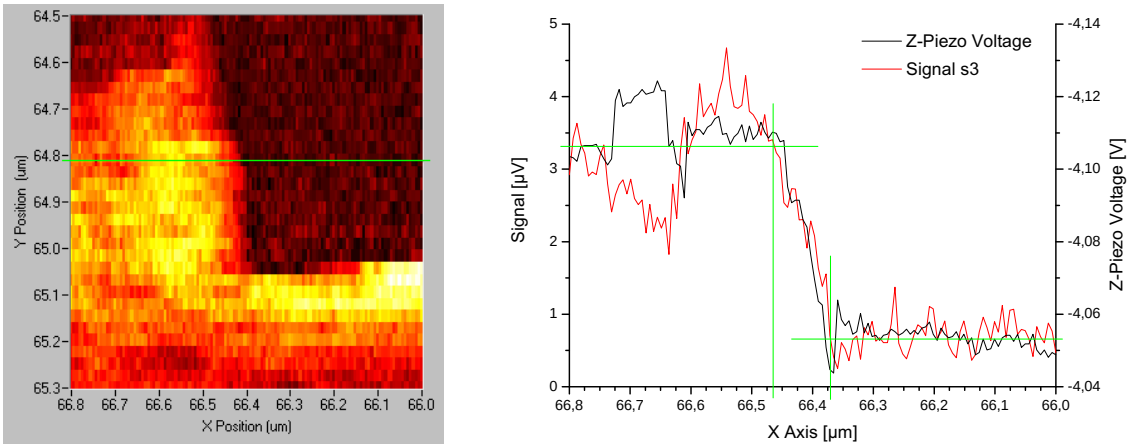

(a) (b)

Figure 5.2: A 800 × 800 nm zoom of the gold pattern shown in figure 5.1. (a) shows the optical signal s3. The illumination wavelength is $\lambda = 2.50$ µm. (b) shows a line scan along the green line indicated in (a).

What can also be seen from the line scan is that the optical resolution is basically the resolution of the of the AFM topography channel. The relatively low resolution of the topography is probably due to the fact that the tip was already used for scanning for more than one day at the time of the scan. With a sharper tip, we expect the instrument to obtain a resolution of $10 - 20$ nm known from other aSNOMs [7].

5.2 Signatures of Optical Resonances

Figure 5.1 already showed that the signal from the gold pattern is not uniform. At the top ends of the structures, the signal is much stronger than elsewhere. In contrast to this, the signal at the lower edges vanishes in the noise.

The asymmetric signal distribution could be related to a tip-asymmetry or to an illumination asymmetry. It may also be an indication that this structure not only gives material contrast but also has some kind of resonance behavior.

Figure 5.3 shows an image of a zoom at the upper left of the structure. At the end of the gold leg, the topography shows no special features. In contrast, the optical signal is much stronger then elsewhere in the structure.

Collective excitations of free charge carriers are known as plasmons, which may efficiently couple to electromagnetic fields, forming plasmon-polaritons whose reso-

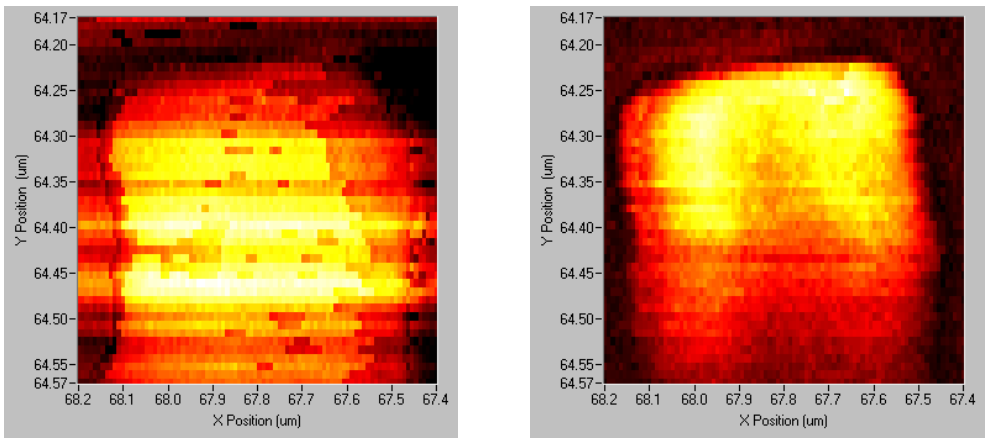

(a) (b)

Figure 5.3: A 800 × 800 µm zoom of the upper left part of the gold pattern shown in figure 5.1. The topography shown in (a) has no special features. (b) shows a strong optical signal s3 at the top of the structure. The illumination wavelength is $\lambda = 2.50$ µm.

nance frequency is characteristic for the dielectric properties of the medium. The so-called surface plasmon-polaritons in particular depend very sensitively on the shape and size of a given sub-wavelength structure [19]. The charge oscillations may lead to a large resonant enhancement of the local field near the surface. This field enhancement is, for example, used in surface-enhanced Raman scattering (SERS). The Raman scattering of molecules on a thin metallic film with atomic-scale roughness can easily be enhanced by a factor of 10^4 – 10^6 [17].

To find out what really causes the strong fields shown in figure 5.3(b), further investigations are needed. To exclude tip asymmetries, we should scan the same structure with a different tip. By changing the illumination direction, for example by rotating the sample, we could verify that the strong optical signal does not originate from an illumination asymmetry. We did no further investigations in this direction because this structure was only a test structure, and we had similar samples with plasmon resonances well-understood by theoretical physicists (see below).

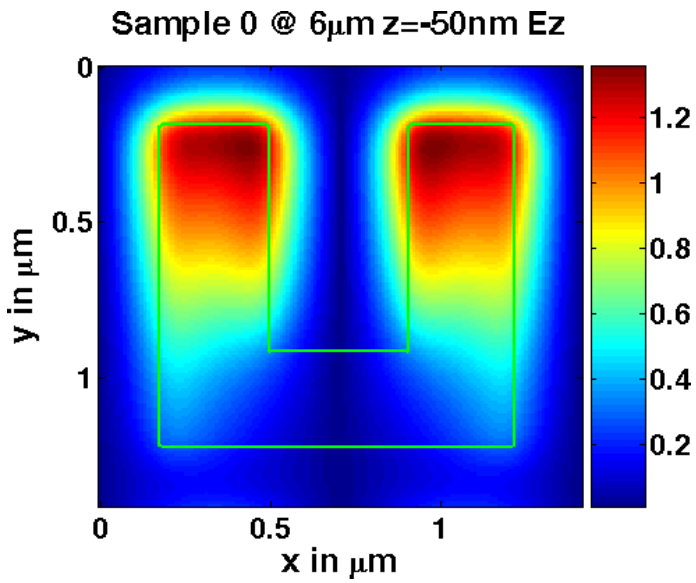

Figure 5.4: Calculated near-fields of a split-ring resonator. The image shows the z-component of the electromagnetic field. The sample is illuminated from the side. The angle between the sample and the illumination beam is 45°.

5.3 First Results with Split Rings

Another sample type we started to investigate are so-called split-rings resonators (SRR) provided by Thomas Zentgraf. In 1999, Pendry proposed to use SSRs much smaller than the wavelength for getting materials with resonant magnetic and dielectric properties [30]. Materials with such properties can have a negative effective index of refraction and may open up a complete new field of optics, perhaps they even will make it possible to build the perfect lens (see [29]). Carsten Rockstuhl et al. started to do systematic research on the optimization of SSRs in the infrared spectrum [33]. They used mainly U-shaped, 20 nm high gold structures with a line width of 60 nm produced by E-beam lithography. They produced different geometries and obtained their far-field reflectivity and absorption in experiment and simulation. The simulations and the experiments were in good agreement. During their studies, they also simulated the near-fields of split-rings. Figure 5.4 shows the predicted electric field in z-direction for an electromagnetic wave polarized along the baseline. The calculated fields shown in figure 5.4 are made for a split-ring of a different size than we used and are thus optimized for a different wavelength. The

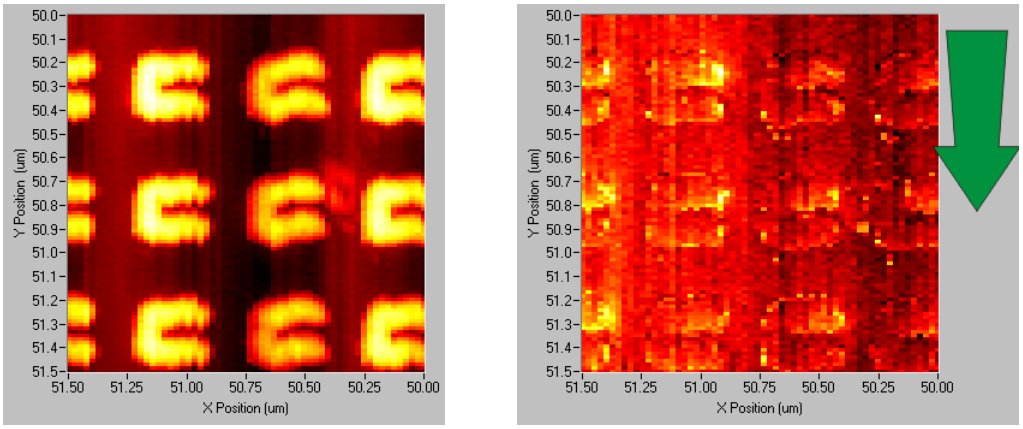

(a) (b)

Figure 5.5: A 1.5×1.5 µm scan of split-ring structures. (a) shows the topography. (b) shows the optical signal s2 measured in second harmonic mode. The green arrow indicates the illumination direction. The illumination wavelength is $\lambda = 2.355$ µm. The fast axis during the scan is the y-axis. The split-rings look a bit distorted because the positioning stage and the sampling device were not synchronized during the scan.

fields of our sample should be similar.

With the resonances of their structures being mainly in the spectral range between 1 and 4 µm, it is an exciting task to check their predictions with the IR-aSNOM. We chose a sample with a base length of 200 nm and a length of each leg of the U being 300 nm long. Fourier-transform infra-red spectrometer measurements showed the strongest reflectance of this sample at a wavelength of 2.5 µm.

For our measurements, we used an uncoated silicon tip[2] to minimize the interaction between tip and sample. The IR-aSNOM is used in passive mode (see section 2.2) and we are able to just *probe* the near-fields around SSRs.

Figure 5.5 shows one of the first images we obtained. Not knowing the exact resonance frequency of the sample at the time, we did our first measurements at a wavelength of 2.355 µm, more than 150 nm away from the resonance peak. The images were taken in second harmonic mode with a tip vibration amplitude of about 20 nm. While the split-ring structures can be clearly seen in the topography image, they hardly give any material contrast in the optical image. Only at the ends of the legs of the structures, strong signals were obtained.

[2]which has a natural SiO_2 layer at the outside

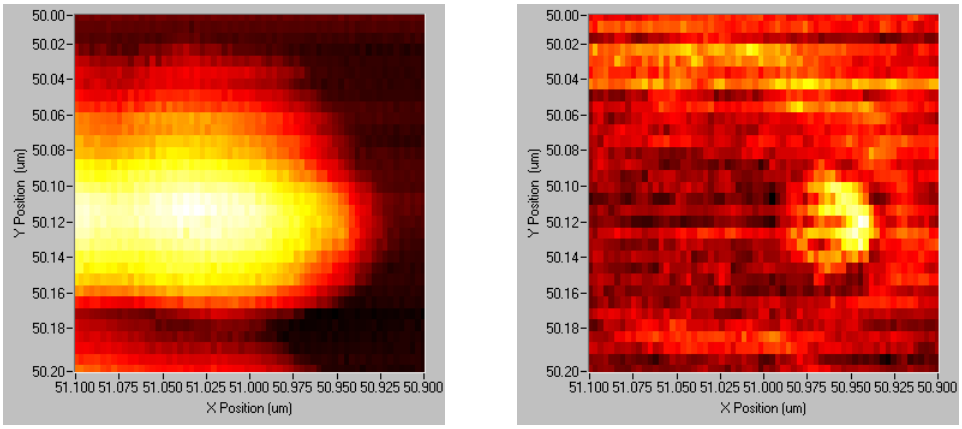

(a) (b)

Figure 5.6: A 200×200 nm scan of the end of a split-ring leg. (a) shows the topography. (b) shows the signal s2. The illumination wavelength is $\lambda = 2.355$ µm.

Figure 5.6 shows a zoom of one of the heads. Although the obtained image matches quite good with the predicted field distribution shown in figure 5.4, these are still preliminary results. We have to do further measurements with different split-ring geometries and at other wavelengths. There is also further theoretical work done at the moment. Thus far, only the near-fields of the SSRs are calculated. Simulations including a metallic tip in small distance over the surface are underway. We will then also be able to compare theory with metallized tip measurements.

6 Outlook

In the last chapters, I showed the theory of the IR-aSNOM, its design, and how it is operated. The idea of the setup is similar to other aSNOMs (for example [2, 13]) which have shown to be reliable tools to obtain optical images beyond the limits of conventional SNOMs . What differentiates the IR-aSNOM from other aSNOMs is the OPO as laser source.

Although being a reliable instrument, it is still not perfect. In this chapter, I present some suggestions to improve and extend the IR-aSNOM.

Now that the new instrument has proven its functional capability, it hopefully starts to produce scientific results. Besides the pure proof of principle, the first measurements have shown interesting optical phenomena that can be investigated with this new instrument. In this chapter, I want to show other interesting applications the IR-aSNOM can be used for.

6.1 Improvements

The initial setup of the instrument after a tip change or selection of a new wavelength, however, is still a time-consuming tedious task that calls for operational improvement. It is desirable to be able to do arbitrary wavelength changes without the need of realignment. The current laser light source forces us to compensate for the different output characteristics of different wavelengths by repositioning the two lenses that parallelize the laser beam. This changes the position and angle of the input beam by a small amount, but this amount is sufficient to require to re-do the focus-finding procedure. To shorten the time between wavelength changes, we plan to build an alignment aid to guarantee exactly the same alignment for different wavelengths, for instance with a spatial filter in between the two mirrors that expand the incoming beam.

As I mentioned at the beginning of chapter 3, we currently do not use the possibility to manipulate the illumination beam and the reference beam separately. In the future, we would like to be able to manipulate the polarization of the two beams separately, possibly with the help of YVO_4 Glen-Taylor-polarizers. We would then be able to also study polarization effects at the nanometer scale with the IR-aSNOM.

6.2 Future Applications

In chapter 5, I already demonstrated the first applications of the IR-aSNOM. Until now, the emphasis was on the proof of principle of the instrument. The gold structures discussed in section 5.1 already showed interesting optical properties not accessible by far-field optics. With the split-ring structures described in section 5.3, we have done first measurements on samples that are well-understood by simulation work. The first measurements point into the direction that the calculated near-fields may be verified with the new instrument. Clearly, further investigations are necessary to prove that the calculations done by Rockstuhl et al. correspond to experimental findings. Interesting aspects include how different aspect ratios of the split-rings change the near-field properties and their wavelength dependence.

Other samples will be interesting from the aspect of material contrast. We hope to be able to show that the IR-aSNOM is able to map material composition of undoped / doped semiconductors. A doped semiconductor has a different dielectric constant and will show a different polarizability of the tip-surface system than an undoped semiconductor. In principle, this should allow to map doping profiles with ≈ 10 nm resolution, which could be a very valuable technique to the semiconductor industry.

The third class of investigations possible with the IR-aSNOM are spectro-microscopic investigations that can be summarized as "chemical microscopy" (see [22]). Many molecules show vibrational absorbance of light in the infrared. With the IR-aSNOM, we can combine the technique of vibrational spectroscopy with the high resolution of an aSNOM. Our laser source, the OS 4000 by Linos, is most often used by chemists to do infrared spectroscopy.

An interesting sample for these investigations might be the tobacco mosaic virus (TMV). It has a tube shape with a diameter of 18 nm and a length of 300 nm. TMVs have been used as templates to synthesize metal nanostructures. By electroless

deposition, metallic nanowires have been produced in the central channel of TMVs, on their outside shell as well as at the ends (see [1, 21]). In terms of optical properties, the amino acids and nucleic acids building the coat proteins have strong absorption bands around a wavelength of 3.3 µm. A comparison of the local spectroscopic response between pristine and metallized TMVs may reveal how these absorption bands shift in the presence of metallic structures.

These are examples of applications for which the IR-aSNOM can give a better insight into the nano-world. With the advances in nano-technology and nano-science, there will probably come up many more in the near future.

Bibliography

[1] Balci, S., Bittner, A.M., Hahn, K., Scheu, C., Knez, M., Kadri, A., Wege, C., Jeske, H., and Kern, K.: *Copper nanowires within the central channel of tobacco mosaic virus particles.* 2006. (submitted).

[2] Bek, A.: *Apertureless SNOM: A New Tool for Nano-Optics.* PhD thesis, École Polytechnique Fédérale de Lausanne, 2004.

[3] Bek, A., Vogelgesang, R., and Kern, K.: *Optical nonlinearity versus mechanical anharmonicity contrast in dynamic mode apertureless scanning near-field optical microscopy.* Applied Physics Letters, 87(163115):1–3, 2005.

[4] Bek, A., Vogelgesang, R., and Kern, K.: *Apertureless scanning near-field optical microscope with sub-10nm resolution.* Review of Scientific Intruments, 2006. (submitted).

[5] Black, E.D.: *An introduction to pound-drever-hall laser frequency stabilization.* American Journal of Physics, 69(1):79–87, January 2001.

[6] Boyd, R.W.: *Nonlinear optics.* In Webb, C.E. and Jones, J.D.C. (eds.): *Handbook of Laser Technology and Applications*, vol. I: Principles, ch. A4, pp. 161–183. Institute of Physics Publishing, London, 2004.

[7] Brehm, M., Frey, H.G., Guckenberger, R., Hillenbrand, R., Kazantsev, D., Keilmann, F., Ocelic, N., and Taubner, T.: *Consolidating apertureless snom.* Journal of the Korean Physical Society, 47:S80–S85, August 2005.

[8] Ebrahimzadeh, M.: *Optical parametric devices.* In Webb, C.E. and Jones, J.D.C. (eds.): *Handbook of Laser Technology and Applications*, vol. II: Laser Design and Laser Systems, ch. C3.2, pp. 1347–1392. Institute of Physics Publishing, London, 2004.

[9] Eichler, J. und Eichler, H. J.: *Laser: Grundlagen, Systeme, Anwendungen.* Laser in Technik und Forschung. Springer–Verlag, Berlin, Heidelberg, New York, 2. Aufl., 1991.

[10] Griffiths, D.J.: *Introduction to Electrodynamics.* Prentice Hall, New Jersey, 3rd ed., 1999.

[11] Hecht, B., Sick, B., Wild, U.P., Deckert, V., Zenobi, R., Martin, O.J.F., and Pohl, D.W.: *Scanning near-field optical microscopy with aperture probes: Fundamentals and applications.* Journal of Chemical Physics, 112(18):7761–7774, 2000.

[12] Hell, S.W., Schrader, M., and Voort, H.T.M. van der: *Far-field fluorescence microscopy with resolution in the 100 nm range.* Journal of Microscopy, 187(1):1–7, 1997.

[13] Hillenbrand, R.: *Nahfeldoptische Amplituden- und Phasenkontrastmikroskopie zur nanoskopischen optischen Abbildung von Materialkontrast und optisch resonanten Partikeln.* Dissertation, Technische Universität München, 2001.

[14] Huang, F.M., Festy, F., and Richards, D.: *Tip-enhanced fluorescence imaging of quantum dots.* Applied Physics Letters, 87(183101):1–3, 2005.

[15] InnoLight GmbH, Garbsener Landstr. 10, 30419 Hannover, Germany: *Mephisto Series User's Manual*, 3.2th ed., 2001.

[16] InnoLight GmbH, Garbsener Landstr. 10, 30419 Hannover, Germany: *Mephisto Product Line*, 2005. `http://www.innolight.de/pdfs/mephisto.pdf`.

[17] Inouye, Y.: *Apertureless metallic probes for near-field microscopy.* In Kawata, S. [18], pp. 29–48.

[18] Kawata, S. (ed.): *Near-field Optics and Surface Plasmon Polaritons*, vol. 81 of *Topics in Applied Physics.* Springer–Verlag, Berlin, Heidelberg, New York, 2001.

[19] Klar, T., Perner, M., Grosse, S., Plessen, G. von, Spirkl, W., and Feldmann, J.: *Surface-plasmon resonances in single metallic nanoparticles.* Physical Review Letters, 80(19):4249–4252, 1998.

[20] Klein, M.V.: *Optics.* John Wiley & Sons, Inc., New York, London, Sydney, Toronto, 1970.

[21] Knez, M., Bittner, A.M., Boes, F., Wege, C., Jeske, H., Maiß, E., and Kern, K.: *Biotemplate synthesis of 3-nm nickel and cobalt nanowires.* Nano Letters, 3(8):1079–1082, 2003.

[22] Knoll, B. and Keilmann, F.: *Near-field probing of vibrational absorption for chemical microscopy.* Nature, 399:134–137, May 1999.

[23] Knoll, B. and Keilmann, F.: *Enhanced dielectric contrast in scattering-type scanning near-field optical microscopy.* Optics Communications, 182:321–328, 2000.

[24] LINOS Photonics GmbH & Co. KG, Isartalstr. 43, 80469 München, Germany: *OS 4000 Operating Manual*, 1.7th ed., 2005.

[25] Lynch, D.W. and Hunter, W.R.: *Optical constants of metals.* In Palik, E. D. [28], pp. 275–367.

[26] Okamoto, T.: *Apertureless near-field probes.* In Kawata, S. [18], pp. 97–122.

[27] Paesler, M.A. and Moyer, P.J.: *Near-field optics: theory, instrumentation, and applications.* John Wiley & Sons, Inc., New York, Chichester, Brisbane, 1996.

[28] Palik, E.D. (ed.): *Handbook of Optical Constants of Solids.* Academic Press, Orlando, 1985.

[29] Pendry, J.B.: *Negative refraction makes a perfect lens.* Physical Review Letters, 85(18):3966–3969, 2000.

[30] Pendry, J.B., Holden, A.J., Robbins, D.J., and Stewart, W.J.: *Magnetism from conductors and enhanced nonlinear phenomena.* IEEE Transactions on Microwave Theory and Techniques, 47(11):2075–2084, 1999.

[31] Philipp, H.R.: *Silicon dioxide (SiO_2) (glass).* In Palik, E. D. [28], pp. 749–763.

[32] Pohl, D.W.: *Near-field optics and the surface plasmon polariton.* In Kawata, S. [18], pp. 1–13.

[33] Rockstuhl, C., Zentgraf, T., Guo, H., Liu, N., Etrich, C., Loa, I., Syassen, K., Kuhl, J., Lederer, F., and Giessen, H.: *Resonances of split-ring resonator metamaterials in the near infrared.* Applied Physics B, 2006.

[34] Schneider, K., Kramper, P., Schiller, S., and Mlynek, J.: *Toward an optical synthesizer: a single-frequency parametric oscillator using periodically poled linbo$_3$.* Optics Letters, 22(17):1293–1295, September 1997.

[35] Siegman, A.E.: *Lasers.* University Science Books, Mill Valley, California, 1991.

[36] Synge, E.H.: *A suggested method for extending microscopic resolution into the ultra-microscopic region.* Philos. Mag., 6:356–362, 1928.

[37] Taubner, T., Hillenbrand, R., and Keilmann, F.: *Performance of visible and mid-infrared scattering-type near-field optical microscopes.* Journal of Microscopy, 210(3):311–314, 2003.

[38] Taubner, T., Keilmann, F., and Hillenbrand, R.: *Effect of tip modulation on image contrast in scattering-type near-field optical microscopy.* Journal of the Korean Physical Society, 47:S213–S216, August 2005.

[39] Thorlabs: *Tools of the Trade*, 17th ed., 2005.

[40] Zenhausern, F., O'Boyle, M.P., and Wickramasinghe, H.K.: *Apertureless near-field optical microscope.* Applied Physics Letters, 65(13):1623–1625, 1994.

Acknowledgements

I thank Professor Klaus Kern for giving me the opportunity to write this thesis within his group at the Max Planck Institute for Solid State Research.

I am grateful to Dr. Ralf Vogelgesang who supervised this thesis. His skills as a mentor, his broad knowledge of optics and his enthusiasm made the work on this thesis so interesting and enjoyable.

I am also grateful to Ruben Esteban who helped me with the work in the lab. His experience was essential to make the IR-aSNOM work.

I would like to thank Dr. Alphan Bek. I gained a great deal of insight from his work on an aSNOM for the visible spectrum.

I would like to thank Thomas Zentgraf for providing the interesting split-ring samples and Dr. Carsten Rockstuhl for providing the theoretical calculations of the split-rings.

I thank Peter Andler, Wolfgang Stiepany and Andreas Koch for their help in producing mechanical parts for the instrument.

And I would like to thank all the other members of the group. Many of them contributed to this work by giving me advice, joining interesting discussions and always being open for questions.

Finally, I would like to thank my family and my girlfriend Brigitte Schultz for supporting me during my studies.